ISTITUTO NAZIONALE DI FISICA NUCLEARE
Laboratori Nazionali di Frascati

FRASCATI PHYSICS SERIES

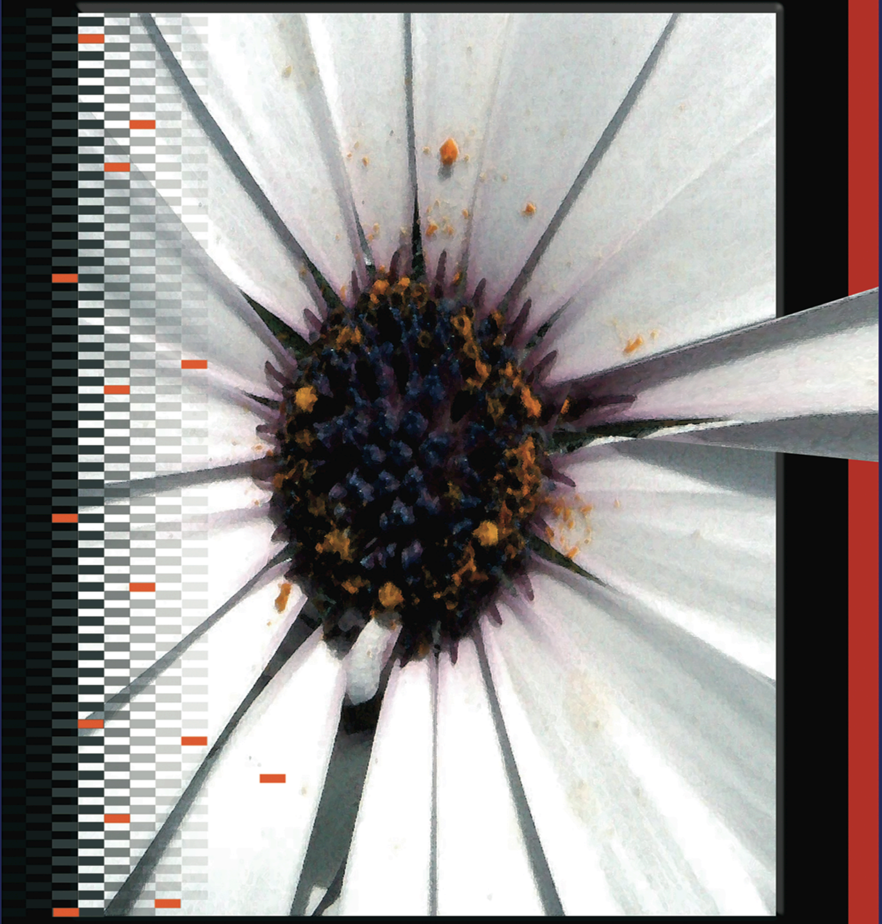

First Young Researchers Workshop
"Physics Challenges in the LHC Era"

2009

Editor
Enrico Nardi

First Young Researchers Workshop
“Physics Challenges in the LHC Era”
2009

FRASCATI PHYSICS SERIES

Series Editor
Danilo Babusci

Technical Editor
Luigina Invidia

Cover by Claudio Federici

Volume XLVIII

Istituto Nazionale di Fisica Nucleare – Laboratori Nazionali di Frascati
Divisione Ricerca
SIDS – Servizio Informazione e Documentazione Scientifica
Ufficio Biblioteca e Pubblicazioni
P.O. Box 13, I–00044 Frascati Roma Italy
email: sis.publications@lnf.infn.it

FRASCATI PHYSICS SERIES

First Young Researchers Workshop
"Physics Challenges in the LHC Era"
2009

ISBN 978–88–86409–57–5

FRASCATI PHYSICS SERIES

Volume XXXVIII

First Young Researchers Workshop
"Physics Challenges in the LHC Era"
2009

Editor
Enrico Nardi

Frascati, May 11th and May 14th, 2009

International Advisory Committee

G. Altarelli	*Università Roma Tre*
W. Buchmuller	*DESY*
F. Ceradini	*Università Roma Tre*
A. Di Ciaccio	*Università Roma Tor Vergata*
J. Ellis	*CERN*
B. Grinstein	*University of California San Diego*
R. Fiore	*Università della Calabria*

Local Organizing Committee

M. Antonelli	*INFN Frascati,*
D. Aristizabal	*INFN Frascati*
O. Cata	*INFN Frascati*
V. Del Duca	*INFN Frascati*
R. Faccini	*Università Roma La Sapienza e INFN Roma*
G. Isidori	*INFN Frascati*
J. F. Kamenik	*INFN Frascati e JSI*
E. Nardi	*INFN Frascati (Chair)*
M. Palutan	*INFN Frascati*
F. Terranova	*INFN Frascati*

PREFACE

The first Young Researcher Workshop "Physics Challenges in the LHC Era" was held in the Frascati Laboratories during May 11th and 14th 2009, in conjunction with the XIV Frascati Spring School "Bruno Touschek".

The main goal of the Workshop was to provide an opportunity for the students attending the Spring School to play an active role in complementing the scientific program by giving short lectures to their colleagues on their specific research topics. In this way the students learn how to organize a presentation on a specialistic subject, so that it will be understandable by an audience of young physicists in the training stage, and how to condense the results of months of research work within a fifteen minutes talk. Helping to develop these skills is an integral part of the scientific formation the Spring School is aiming to.

The Workshop was very successful, both in its scientific and formative aspects. Despite that for many of the sixteen young speakers this was the first public presentation of their researches, all the talks reflected a remarkably high professional level, and could have well fitted within the scientific program of many international conferences.

These proceedings, that collect the joint efforts of the speakers of the Young Researchers Workshop, aim to set a benchmark for the scientific level required to participate in future editions of the Workshop. It will also provide useful guidelines for structuring the presentations of our next set of young lecturers.

Too many people contributed to the success of the Young Researcher Workshop "Physics Challenges in the LHC Era" and of the joint XIV Frascati Spring School "Bruno Touschek" to give here a complete list. However, a special acknowledgment must be given to the Workshop secretariat staff and backbones of the Frascati Spring School Maddalena Legramante and Angela Mantella, to Claudio Federici, that put a special effort in realizing the graphics of the Workshop and School posters, to Luigina Invidia for the technical editing of these proceedings, and to the Director of the Frascati Laboratories Mario Calvetti for constant encouragement and support.

Frascati, July 2009 Enrico Nardi

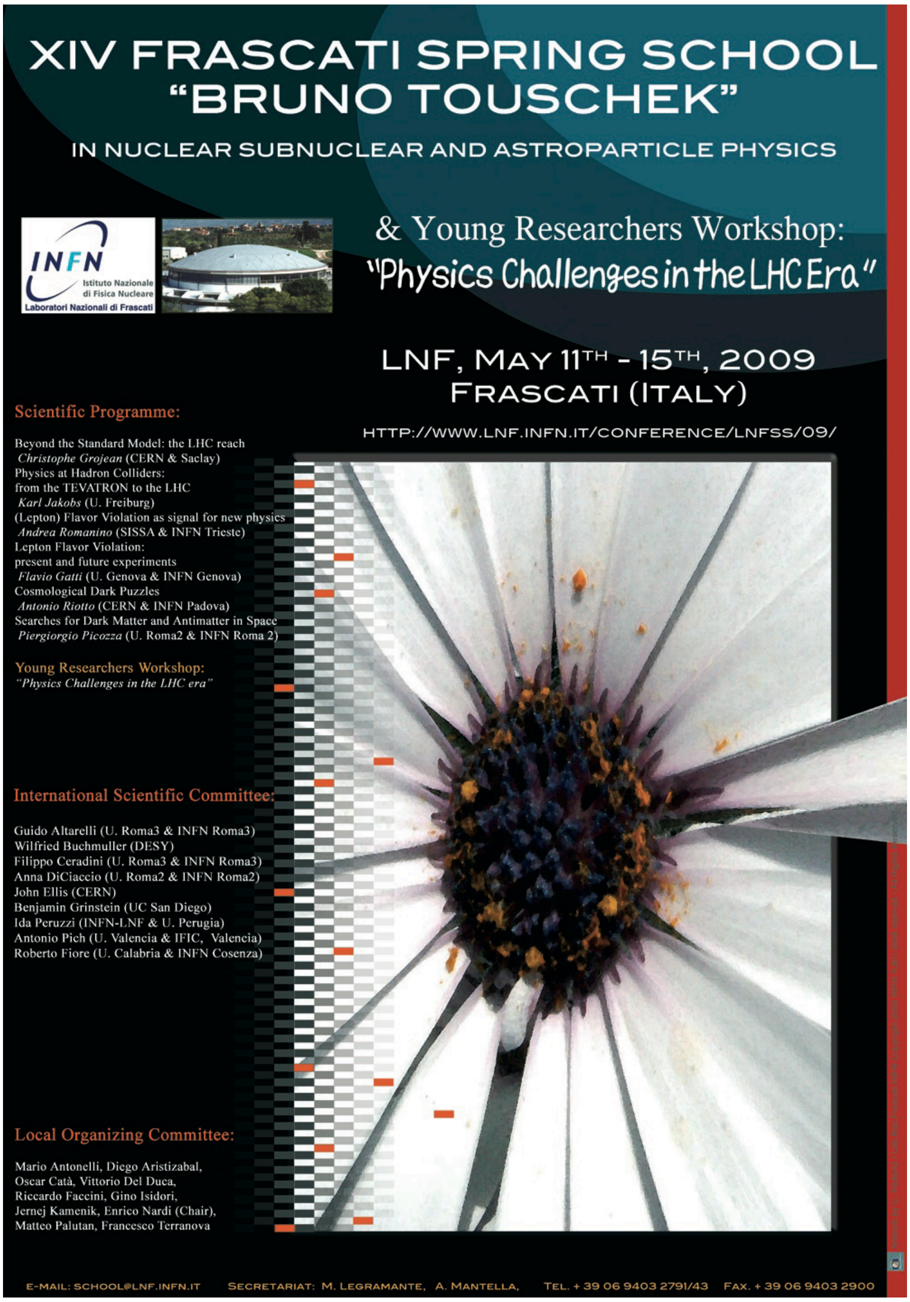

XIV FRASCATI SPRING SCHOOL "BRUNO TOUSCHEK"

IN NUCLEAR SUBNUCLEAR AND ASTROPARTICLE PHYSICS

& Young Researchers Workshop: "Physics Challenges in the LHC Era"

LNF, MAY 11TH - 15TH, 2009
FRASCATI (ITALY)

HTTP://WWW.LNF.INFN.IT/CONFERENCE/LNFSS/09/

Scientific Programme:

Beyond the Standard Model: the LHC reach
Christophe Grojean (CERN & Saclay)
Physics at Hadron Colliders:
from the TEVATRON to the LHC
Karl Jakobs (U. Freiburg)
(Lepton) Flavor Violation as signal for new physics
Andrea Romanino (SISSA & INFN Trieste)
Lepton Flavor Violation:
present and future experiments
Flavio Gatti (U. Genova & INFN Genova)
Cosmological Dark Puzzles
Antonio Riotto (CERN & INFN Padova)
Searches for Dark Matter and Antimatter in Space
Piergiorgio Picozza (U. Roma2 & INFN Roma 2)

Young Researchers Workshop:

"Physics Challenges in the LHC era"

International Scientific Committee:

Guido Altarelli (U. Roma3 & INFN Roma3)
Wilfried Buchmuller (DESY)
Filippo Ceradini (U. Roma3 & INFN Roma3)
Anna DiCiaccio (U. Roma2 & INFN Roma2)
John Ellis (CERN)
Benjamin Grinstein (UC San Diego)
Ida Peruzzi (INFN-LNF & U. Perugia)
Antonio Pich (U. Valencia & IFIC, Valencia)
Roberto Fiore (U. Calabria & INFN Cosenza)

Local Organizing Committee:

Mario Antonelli, Diego Aristizabal,
Oscar Catà, Vittorio Del Duca,
Riccardo Faccini, Gino Isidori,
Jernej Kamenik, Enrico Nardi (Chair),
Matteo Palutan, Francesco Terranova

E-MAIL: SCHOOL@LNF.INFN.IT   SECRETARIAT: M. LEGRAMANTE, A. MANTELLA,   TEL. + 39 06 9403 2791/43   FAX. + 39 06 9403 2900

Artwork by Claudio Federici

CONTENTS

Frascati Physics Series Vol. XLVIII (2009), pp. 1-6
Young Researchers Workshop: *“Physics Challenges in the LHC Era”*
Frascati, May 11 and 14, 2009

QCD AMPLITUDES WITH THE GLUON EXCHANGE AT HIGH ENERGIES (AND GLUON REGGEIZATION PROOF)

A.V. Reznichenko
Budker Institute of Nuclear Physics, 630090 Novosibirsk, Russia
M.G. Kozlov
Novosibirsk State University, 630090 Novosibirsk, Russia

Abstract

We demonstrate that the multi-Regge form of QCD amplitudes with gluon exchanges is proved in the next-to-leading approximation. The proof is based on the bootstrap relations, which are required for the compatibility of this form with the s-channel unitarity. It was shown that the fulfillment of all these relations ensures the Reggeized form of energy dependent radiative corrections order by order in perturbation theory. Then we prove that all these relations are fulfilled if several bootstrap conditions on the Reggeon vertices and trajectory hold true. All these conditions are checked and proved to be satisfied for all possible t-channel color representations. That finally completes the proof of the gluon Reggeization in the next-to-leading approximation and provides the firm basis for BFKL approach therein.

1 Introduction

Reggeization of gluons as well as quarks is one of remarkable properties of Quantum Chromodynamics (QCD). The gluon Reggeization is especially important since cross sections non vanishing in the high energy limit are related to gluon exchanges in cross channels. A primary Reggeon in QCD turns out to be the Reggeized gluon.

The gluon Reggeization gives the most common basis for the description of high energy processes. In particular, the famous BFKL equation $^{1)}$ was derived supposing the Reggeization. The most general approach to the unitarization problem is the reformulation of QCD in terms of a gauge-invariant effective field theory for the Reggeized gluon interactions.

The gluon Reggeization was proved in the leading logarithmic approximation (LLA), i.e. in the case of summation of the terms $(\alpha_S \ln s)^n$ in cross-sections of processes at energy $\sqrt{s}$ in the c.m.s., but till now remains a hypothesis in the next-to-leading approximation (NLA), when the terms $\alpha_S(\alpha_S \ln s)^n$ are also kept. Now the BFKL approach $^{1)}$, based on the gluon Reggeization, is intensively developed in the NLA.

We present the proof of the gluon Reggeization in the NLA. Substantially in our consideration we follow the paper $^{2)}$. All references are presented therein. First we show that the fulfillment of the bootstrap relations guarantees the multi–Regge form of QCD amplitudes. Then we demonstrate that an infinite set of these bootstrap relations are fulfilled if several conditions imposed on the Reggeon vertices and the trajectory (bootstrap conditions) hold true. Now almost all these conditions are proved to be satisfied. In our consideration we hold the following terminology:

Multi-Regge kinematics (MRK). Let us consider the amplitude (see fig.1) $\mathcal{A}_{2\to n+2}$ of the process $A + B \to A' + J_1 + \ldots + J_n + B'$: see the figure. We use light-cone momenta n_1 and n_2, with $n_1^2 = n_2^2 = 0, \;\; (n_1 n_2) = 1$, and denote $(pn_2) \equiv p^+, \;\; (pn_1) \equiv p^-$. Let assume that initial momenta p_A and p_B have predominant components p_A^+ and p_B^-. MRK supposes that rapidities of final jets J_i with momenta k_i $y_i = \frac{1}{2}\ln\left(k_i^+/k_i^-\right)$ decrease with i: $y_0 > y_1 > \ldots > y_n > y_{n+1}$; as for y_0 and y_{n+1}, it is convenient to define them as $y_0 = y_A \equiv \ln\left(\sqrt{2}p_A^+/|q_{1\perp}|\right)$ and $y_{n+1} = y_B \equiv \ln\left(|q_{(n+1)\perp}|/\sqrt{2}p_B^-\right)$. Notice that q_i indicate the Reggeon momenta and $q_1 = p_{A'} - p_A \equiv q_A$, $q_{n+1} = p_B - p_{B'} \equiv q_B$.

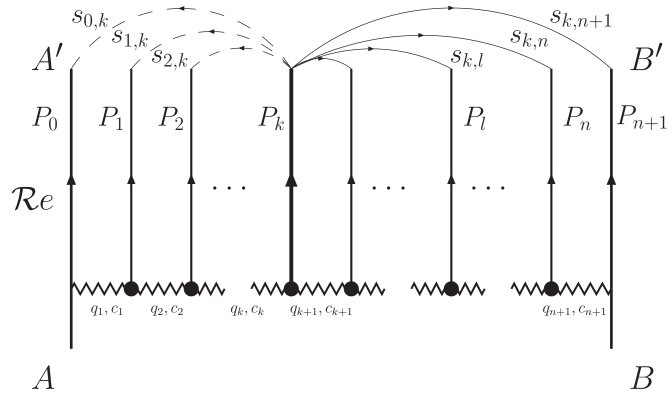

Figure 1: *The amplitude for the process* $2 \to n+2$*.*

Signature in the channel t_l for multi-particle production means the symmetrization (or antisymmetrization) with respect to the substitution $s_{i,j} \leftrightarrow -s_{i,j}$, for $i < l \leq j$. Here $s_{i,j} = (k_i + k_j)^2$.

Hypothesis of the gluon reggeization claims that in MRK the real part of the NLA-amplitude $2 \to n+2$ with negative signature has universal form, where all energy dependence is exponentiated:

$$\Re \mathcal{A}_{AB}^{A'B'+n} = \bar{\Gamma}_{A'A}^{R_1} \left(\prod_{i=1}^{n} \frac{e^{\omega(q_i^2)(y_{i-1}-y_i)}}{q_{i\perp}^2} \gamma_{R_i R_{i+1}}^{J_i} \right) \frac{e^{\omega(q_{n+1}^2)(y_n-y_{n+1})}}{q_{(n+1)\perp}^2} \Gamma_{B'B}^{R_{n+1}}, \quad (1)$$

where $y_i = \frac{1}{2} \ln(\frac{k_i^+}{k_i^-})$ — particle (P_i) rapidities, and $\gamma_{R_i R_{i+1}}^{J_i}$, $\Gamma_{P'P}^{R}$ — known effective vertices, and $\omega(q_i^2)$ — (perturbatively) known gluon trajectory.

2 The concept of the gluon Reggeization proof

Using the elementary properties of the signaturized NLO amplitude we can obtain the following bootstrap relations:

$$\Re\Big(\sum_{l=k+1}^{n+1} \mathrm{disc}_{s_{k,l}} - \sum_{l=0}^{k-1} \mathrm{disc}_{s_{l,k}} \Big) \frac{\mathcal{A}_{AB}^{A'B'+n}}{-2\pi i} = \frac{1}{2}(\omega(t_{k+1}) - \omega(t_k)) \Re \mathcal{A}_{AB}^{A'B'+n}. \quad (2)$$

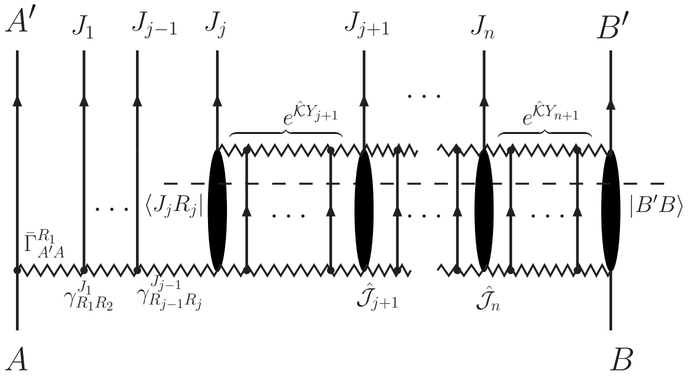

Figure 2: $s_{j,n+1}$-*channel discontinuity calculation via unitarity relation.*

These relations constitute an infinite number of necessary and sufficient conditions for compatibility of the Regge amplitude form (eq.1) with unitarity: the discontinuities (see fig.2) in these relations must be calculated using the s–channel unitarity and the multi-Regge form of the amplitudes (eq.1). Evidently, there is an infinite number of the bootstrap relations, because there is an infinite number of amplitudes $\mathcal{A}_{2\to n+2}$.

3 Bootstrap conditions

An infinite number of the bootstrap relations (eq.2) are satisfied if the finite number of following bootstrap conditions are fulfilled. In $^{2)}$ we show that the fulfilment of the bootstrap conditions guarantees the implementation of all the infinite set of the bootstrap relations (eq.2). These conditions can be divided into two sorts: elastic and inelastic ones.

Elastic bootstrap conditions describe the properties of the transition of the initial particle B to B' with the two Reggeon emission in the t channel: see the rightmost blob in fig2. In Reggeon operator formalism $^{2)}$ the impact factors for scattering particles satisfy equations

$$|\bar{B}'B\rangle = g\Gamma^{R_{n+1}}_{B'B}|R_\omega(q_{B\perp})\rangle, \;\; \langle A'\bar{A}| = g\bar{\Gamma}^{R_1}_{A'A}\langle R_\omega(q_{A\perp})|, \tag{3}$$

where $\langle R_\omega(q_\perp)|$ and $|R_\omega(q_\perp)\rangle$ are the *bra*– and *ket*– vectors of the universal (process independent) eigenstate of the BFKL kernel $\hat{\mathcal{K}}$ with the eigenvalue $\omega(q_\perp)$,

$$\hat{\mathcal{K}}|R_\omega(q_\perp^2)\rangle = \omega(q_\perp^2)|R_\omega(q_\perp)\rangle, \;\; \langle R_\omega(q_\perp^2)|\hat{\mathcal{K}} = \langle R_\omega(q_\perp)|\,\omega(q_\perp^2), \tag{4}$$

The last equations give us elastic bootstrap conditions. The bootstrap conditions (eq.3) and (eq.4) are known since a long time and have been proved to be satisfied about ten years ago.

Inelastic bootstrap conditions connect the Reggeon-gluon impact factors (the leftmost blob in fig.2) and the gluon production operator (the centre blobs in fig.2). In our formalism these conditions can be written in the following universal form:

$$\hat{\mathcal{J}}_i\,|R_\omega(q_{(i+1)\perp})\rangle\, g\, q^2_{(i+1)\perp} + |\bar{J}_i R_{i+1}\rangle = |R_\omega(q_{i\perp})\rangle\, g\, \gamma^{J_i}_{R_i R_{i+1}}. \tag{5}$$

The first term is referred to as the operator of the jet J_i production. In our approximation (NLA) the jet J_i is either one gluon, or quark-antiquark pair (or two gluons) with close rapidities. The operator of the jet production $\langle \mathcal{G}_1' \mathcal{G}_2' | \hat{\mathcal{J}}_i\,|R_\omega(q_{(i+1)\perp})\rangle$ (i.e. operator $\hat{\mathcal{J}}_i$ projected onto the two-Reggeon t-channel state $\langle \mathcal{G}_1' \mathcal{G}_2'|$ and onto kernel eigenstate $|R_\omega(q_{i\perp})\rangle$) can be explicitly viewed 2) through known in NLO effective vertices and the gluon trajectory. The second element $\langle \mathcal{G}_1' \mathcal{G}_2' | \bar{J}_i R_{i+1}\rangle$ of (eq.5) is the impact-factor of the jet production. It describes the transition of the t-channel Reggeon R_{i+1} into the final jet J_i and two-Reggeon t-channel state. The analytical form through the effective vertices and the trajectory one can find in 2). For the case when the jet J_i is quark-antiquark pair or two gluons the bootstrap condition (eq.5) was proved several years ago 3). The last unproved bootstrap condition reproduces the case when J_i is one gluon.

From the explicit form of the effective vertices it is easy to see that for the gluon contribution there are only three independent colour structures that lead to the nontrivial bootstrap condition. The optimal choice is the “trace-based”:

$$\mathrm{Tr}[T^{c_2}T^aT^{c_1}T^i], \;\; \mathrm{Tr}[T^aT^{c_2}T^{c_1}T^i], \;\; \mathrm{Tr}[T^aT^{c_1}T^{c_2}T^i], \tag{6}$$

where a is a colour index of the external gluon; i is a colour index of one-Reggeon t-channel state, and c_1, c_2 are colour indices of the two-Reggeon t-channel state. Two years ago by the direct loop calculation we demonstrated that the inelastic bootstrap condition was fulfilled being projected onto the colour octet in the

t-channel. For the quark contribution all bootstrap conditions can be obtained from the octet one and thereby are fulfilled.

The bootstrap conditions for the second and third colour structures in (eq.6) can be obtained from the octet one in a simple way. The first colour structure (symmetric with respect to c_1 and c_2) is essentially new.

Up to date by the direct loop calculation in the dimensional regularization we found both impact-factor and operator of the gluon production, and checked the cancellation of all singular (collinear and infrared singularities), logarithmic, and rational terms within the bootstrap condition for this structure. The matter of the nearest future is to cancel all dilogarithmic and double logarithmic terms. That will accomplish the NLA gluon reggeization proof irreversibly.

4 Conclusion

We presented the basic steps of the proof that in the multi–Regge kinematics real parts of QCD amplitudes for processes with gluon exchanges have the simple multi-Regge form.

The proof is based on the bootstrap relations required by the compatibility of the multi–Regge form (eq.1) of inelastic QCD amplitudes with the s–channel unitarity.

References

1. V.S. Fadin, E.A. Kuraev and L.N. Lipatov, Phys. Lett. B **60**, 50 (1975).
2. V.S. Fadin, R. Fiore, M.G. Kozlov, A.V. Reznichenko, Phys. Lett. **B**, 639 (2006)
3. V.S. Fadin, M.G. Kozlov and A.V. Reznichenko, Yad. Fiz. **67**, 377 (2004).

Frascati Physics Series Vol. XLVIII (2009), pp. 7-12
YOUNG RESEARCHERS WORKSHOP: *“Physics Challenges in the LHC Era”*
Frascati, May 11 and 14, 2009

INCLUDING QCD RADIATION CORRECTIONS IN TRANSPLANCKIAN SCATTERING

Paolo Lodone
Scuola Normale Superiore of Pisa and INFN

Abstract

The hypothesis of models with Large Extra Dimensions is that the fundamental Planck scale can be lowered down to some TeV if gravity propagates in some (compactified) extra dimensions. If this is the case, quantum gravity effects could be visible at the LHC. Gian F. Giudice *et al* in 1) studied these effects in the eikonal approximation. It is interesting both from a phenomenological and a theoretical point of view to study the corrections to these results due to the QCD radiation. To evaluate this contribution, we generalize a shock-wave method proposed by 't Hooft, so that we are able to obtain the amplitude at first order in QCD corrections but resummed at all orders in gravity. Studying this result we can learn many interesting things, for example we can extract the true scale of the process. This is actually work in progress jointly with Vyacheslav Rychkov, the complete results will appear in 2).

1 Introduction

The hypothesis [3] of Large Extra Dimensions (LED) is motivated by the Hierarchy problem and amounts to suppose that there exists n compactified extra dimensions so that the Einstein - Hilbert action of General Relativity (GR) becomes, with $D = 4 + n$:

$$S_D = \frac{1}{2} \int d^D x \sqrt{-g^{(D)}} M_D^{n+2} R^{(D)}. \tag{1}$$

Integrating out these extra dimensions we obtain:

$$M_{Pl}^2 = M_D^{2+n} (2\pi r)^n \tag{2}$$

where r is the size of the extra dimensions in the simplest case of toroidal compactification. This means that if the volume of the compactified extra dimensions is “large”, then the scale M_D at which Quantum Gravity (QG) should manifest itself is much lower then the usual Planck scale M_{Pl}.

The important point (see [4] for a review) is that if we assume that only gravity can propagate in the n extra dimensions, then the only observable effect is a deviation from the newtonian potential at distances smaller than r. Moreover setting $M_D = 1$ TeV we have $r = 2 \cdot 10^{-16} 10^{\frac{32}{n}}$ mm. Since the experimental data impose $r \leq 0.2$ mm, we immediatly see that:

$$n \geq 2 \qquad , \qquad M_D \approx 1 \text{ TeV} \tag{3}$$

is a serious possibility which has to be taken into account at the LHC.

2 Transplanckian scattering

Let us consider the case of scattering events, following [1]. Defining the D-dimensional gravitational coupling constant as $G_D = \frac{(2\pi)^{n-1} \hbar^{n+1}}{4 c^{n-1} M_D^{n+2}}$, the relevant length scales are:

$$\lambda_B = \frac{4\pi\hbar c}{\sqrt{s}} \quad , \quad \lambda_P = \left(\frac{G_D \hbar}{c^3} \right)^{\frac{1}{n+2}} \quad , \quad R_S = \frac{1}{\sqrt{\pi}} \left[\frac{8\Gamma(\frac{n+3}{2})}{n+2} \right]^{\frac{1}{n+1}} \tag{4}$$

where λ_B is the de Broglie wavelength, λ_P is the Planck scale (at which QG appears), and R_S is the Schwarzschild radius (at which curvature effects become large). It is important to notice that in this D-dimensional framework we also have the length scale:

$$b_c = \left(\frac{G_D s}{\hbar c^5}\right)^{\frac{1}{n}} \tag{5}$$

which can not be defined if $n = 0$ and moreover goes to infinity if $\hbar \to 0$ with G_D fixed. This means that b_c is related to the size of the classical region in the impact parameter space.

Since the true theory of QG is not known, we are interested in model independent predictions. First of all let us assume that $b_c \gg R_S$, which is certainly true at sufficiently high energy. Notice that for impact parameter $b \gg R_S$ gravity can be linearized. Moreover if $\sqrt{s} \gg M_D$ then $R_S \gg \lambda_P \gg \lambda_B$, which means that QG effects are expected to be small. Finally, in the case of forward scattering at small angles, we are able to perform a predictive computation using the eikonal resummation or the shock-wave method, as we will see in the following sections. In conclusion, in the transplanckian eikonal regime defined by:

$$\sqrt{s} \gg M_D \qquad , \qquad \frac{-t}{s} \ll 1 \tag{6}$$

it is possible to obtain model independent predictions which rely only on Quantum Mechanics (QM) and linearized GR. Notice that all this can be of interest only in a LED scenario with the QG scale M_D lowered down to a few TeV.

3 Eikonal amplitude without radiation

As shown in 1) and 5), a first approach for the evaluation of the transplanckian eikonal amplitude is "eikonalization", which amounts to resum an infinite number of Feynman diagrams with graviton exchanges which are one by one ultraviolet (UV) divergent but whose sum is finite. In performing this sum we neglect the virtuality of gravitons in the matter propagators and we make use of the on-shell vertices. The final result is:

$$\mathcal{A}_{eik}(q_\perp) = -2is \int d^2 b_\perp e^{iq_\perp b_\perp} (e^{i\chi(b_\perp)} - 1) \tag{7}$$

where $q_\perp$ is the momentum transfer, which is mainly transverse ($q_\perp^2 \approx -t$), and:

$$\chi(b_\perp) = \frac{1}{2s} \int \frac{d^2 q_\perp}{(2\pi)^2} e^{-iq_\perp b_\perp} \mathcal{A}_{tree}(q_\perp) = \left(\frac{b_c}{b_\perp}\right)^n . \tag{8}$$

Notice that this amplitude is spin independent and moreover there is no UV sensitivity. This means that in this regime we can obtain a prediction in perturbative QG which does not depend on the way QG is regolarized.

An equivalent approach which shows even more explicity the fact that this prediction relies only on QM and GR is 't Hooft shock wave method 6). In this case we solve the Einstein equations for a very energetic particle, obtaining the Aichelburg-Sexl shock wave metric 7):

$$ds^2 = -dx^+dx^- + \Phi(x_\perp)\delta(x^-)(dx^-)^2 + dx_\perp^2 \tag{9}$$

where the particle is moving in the positive z direction, and:

$$\begin{aligned} \frac{\Phi}{8\pi G_D} &= -\frac{E}{\pi}\log|x_\perp| && \text{if } D = 4 \\ &= \frac{2\,\Gamma(\frac{k+1}{2})\,E}{2\,\pi^{\frac{k+1}{2}}\,(D-4)\,|x_\perp|^{D-4}} && \text{if } D > 4\,. \end{aligned} \tag{10}$$

We can perform a (discontinuous) coordinate transformation $x \to x'$ in order to make the metric continuous across $x^- = 0$. At $x^- = x'^- = 0$ we have:

$$\begin{cases} x^+ = x'^+ + \theta(x^-)\,\Phi(x_\perp) \\ x^i = x'^i \qquad (i = 1, 2)\ . \end{cases} \tag{11}$$

Then we solve the equations of motion for the other particle in this shock-wave spacetime, which consists of two flat semispaces glued together at $x^- = 0$ with the discontinuity (11). For a particle with energy E moving in the negative z direction ($p = (E, -E, 0)$) the wavefuction is, before the collision:

$$\psi(x) = e^{-ipx} = e^{-iEx^+} \qquad (x^- < 0) \tag{12}$$

while immediatly after the collision the continuity in the x' coordinates implies:

$$\psi(x) = e^{-iE(x^+ - \Phi(x_\perp))} \qquad (x^- \to 0^+) \tag{13}$$

thus we obtain the eikonal amplitude:

$$\mathcal{A}_{eik}(x_\perp) = e^{iE\Phi(x_\perp)}. \tag{14}$$

It can be checked 2) that $E\Phi(x_\perp)$ is exactly the eikonal $\chi(x_\perp)$ of (8). Notice that the -1 in (7) gives a contribution proportional to $\delta(q_\perp)$, and the overall factors can be obtained by properly normalizing the wavefunctions.

4 Including radiation

In order to compute the QCD radiation corrections to the amplitude (7), the best way to proceed is to generalize 't Hooft method using the Green's functions for the various particles in the shock-wave spacetime. Let us consider for simplicity a scalar quark with momentum p which scatters across the shock wave changing its momentum into p' and emitting a gluon with momentum l. Then apart from some normalization factors the matrix element is:

$$M_{p\rightarrow p'+l} = \int d^4x\sqrt{-g}g^{\mu\nu}G_{out}(p',x)\overleftrightarrow{\partial}_{\mu}G_{in}(x,p)G^{A}_{out}(l,\varepsilon,x)_{\nu}. \tag{15}$$

The Green's functions are obtained via 't Hooft method, for example for the incoming quark $G_{in}(x,p) = e^{-ipx}$ for $x^- < 0$ while for $x^- > 0$ we have:

$$G_{in}(x,p) = \int \frac{d^2k^i}{(2\pi)^2} e^{-i(\frac{(p^i+k^i)^2}{2p^-}x^- + \frac{p^-}{2}x^+ - (p^i+k^i)x^i)} A(k^i,p^-) \tag{16}$$

where:

$$e^{i\frac{p^-}{2}\Phi(x^i)} = \int \frac{d^2k}{(2\pi)^2} e^{ik^ix^i} A(k^i,p^-). \tag{17}$$

The only subtlety is that for the case of the gluon (photon) Green's function we must include the Jacobian of the transformation (11) at $x^- = 0$, which can be found in 8). All these details can be found in 2). The final result is $M = \int_{x^-<0} + \int_{x^->0} = M_- + M_+$, with:

$$M_+ = (2\pi)\delta(p'^- - p^- + l^-)\frac{2(p'+\tilde{p})^{\mu}\varepsilon_{\mu}}{(p'^+ - \tilde{p}^+ + l^+) + i\epsilon}A(p'_{\perp} - p_{\perp} + l_{\perp}, p^-) \tag{18}$$

$$\begin{aligned} M_- &= (2\pi)\delta(p'^- - p^- + l^-)\int \frac{d^2k_{\perp}}{(2\pi)^2}\frac{2(\tilde{p}'+p)^{\mu}\tilde{\varepsilon}_{\mu}}{-(\tilde{p}'^+ - p^+ + \tilde{l}^+) + i\epsilon} \times \\ &\times A((p'-p+l-k)_{\perp}, p'^-)A(k_{\perp}, l^-) \end{aligned} \tag{19}$$

$(\tilde{p}^+, \tilde{p}^-, \tilde{p}_{\perp}) = (\frac{(p'_{\perp}+l_{\perp})^2}{p^-}, p^-, p'_{\perp}+l_{\perp})$, $(\tilde{p}'^+, \tilde{p}'^-, \tilde{p}'_{\perp}) = (\frac{(p_{\perp}-\tilde{l}_{\perp})^2}{p'^-}, p'^-, p_{\perp}-\tilde{l}_{\perp})$, and $\tilde{\varepsilon}_{\mu}$ is the transformed of ε_{μ} through the Jacobian of (11). It can be checked that gauge invariance holds.

As a first application of this result, we can determine the scale of the process by studying the large logarithms coming from $\int d^2l\,|M|^2$. What we find is that, in the case of large momentum transfer $b_c q_{\perp} \gg 1$, if we want to reabsorb the large corrections the scale at which the parton distribution functions must be normalized is:

$$Q_{eff} = \frac{(q_\perp b_c)^{\frac{1}{n+1}}}{b_c} \,. \tag{20}$$

Notice that for $n = 0$ the scale lenght b_c cannot be defined, and in fact in this case there is no “strange behaviour”. It is interesting to note also that this scale is essentially the inverse of the impact parameter that dominates the amplitude (7) in the stationary phase approximation, which is named b_s in 1).

5 Conclusions and perspectives

For the moment the main result of this study is the generalization of ’t Hooft method 6) in order to include QCD radiation in transplanckian scattering. The sum of (18) and (19), apart from some normalization factors, gives $M_{p\to p'+l}$ at the first order in QCD and at all orders in gravity in the regime (6). We have also hints about the true scale of this process, which may not be just the momentum transfer. In 2) we will derive all this in full detail and we will carefully study the implications for signals at colliders.

6 Acknowledgements

In this project I am working jointly with Vyacheslav Rychkov, whom I thank.

References

1. G.F. Giudice *et al*, Nucl. Phys. B **630** 293-325 (2002).
2. P. L., V. Rychkov, *QCD Radiation in transplanckian scattering*, to appear.
3. N. Arkani-Hamed *et al*, Phys. Lett. B **429**, 263 (1998).
4. C. Csáki, [arXiv:hep-ph/0404096]; G.D. Kribs, [arXiv:hep-ph/0605325].
5. D. Kabat *et al*, Nucl. Phys. B **388**, 570 (1992).
6. G. ’t Hooft, Phys. Lett. B **198**, 61 (1897).
7. P.C. Aichelburg *et al*, Gen. Rel. Grav. **2**, 303 (1971).
8. V. Rychkov, Phys. Rev. D **70** 044003 (2004).

Frascati Physics Series Vol. XLVIII (2009), pp. 13-18
YOUNG RESEARCHERS WORKSHOP: *"Physics Challenges in the LHC Era"*
Frascati, May 11 and 14, 2009

PURELY FLAVORED LEPTOGENESIS AT THE TeV SCALE

Luis Alfredo Muñoz
Instituto de Física, Universidad de Antioquia, A.A. 1226, Medellín, Colombia

Abstract

I study variations of the standard leptogenesis scenario that can arise if an additional mass scale related to the breaking of some new symmetry is present below the mass M_{N_1} of the lightest right-handed Majorana neutrino. I present a particular realization of this scheme that allows for leptogenesis at the TeV scale. In this realization the baryon asymmetry is exclusively due to flavor effects.

1 Introduction

From observations of light element abundances and of the Cosmic microwave background radiation (1) the Cosmic baryon asymmetry, $Y_B = \frac{n_B - n_{\bar{B}}}{s} = (8.75 \pm 0.23) \times 10^{-10}$, (where s is the entropy density) can be inferred. The conditions for a dynamical generation of this asymmetry (baryogenesis) are well known [2)] and depending on how they are realized different scenarios for baryogenesis can be defined (see ref. [3)] for a througout discussion). Leptogenesis [4)] is a scenario in which an initial lepton asymmetry, generated in the out-of-equilibrium decays of heavy singlet Majorana neutrinos (N_α), is partially converted in a baryon asymmetry by anomalous sphaleron interactions [5)] that are standard model processes. Singlet Majorana neutrinos are an essential ingredient for the generation of light neutrino masses through the seesaw mechanism [6)]. This means that if the seesaw is the source of neutrino masses then qualitatively, leptogenesis is unavoidable. Consequently, whether the baryon asymmetry puzzle can be solved within this framework turn out to be a quantitative question. This has triggered a great deal of interest on quantitative analysis of the standard leptogenesis model and indeed a lot of progress during the last years has been achieved (see ref. [7)]).

2 The Model

The model we consider here [8)] is a simple extension of the standard model containing a set of $SU(2)_L \times U(1)_Y$ fermionic singlets, namely three right-handed neutrinos ($N_\alpha = N_{\alpha R} + N^c_{\alpha R}$) and three heavy vectorlike fields ($F_a = F_{aL} + F_{aR}$). In addition, we assume that at some high energy scale, taken to be of the order of the leptogenesis scale M_{N_1}, an exact $U(1)_X$ gauge horizontal symmetry forbids direct couplings of the lepton ℓ_i and Higgs Φ doublets to the heavy Majorana neutrinos N_α. At lower energies, $U(1)_X$ gets spontaneously broken by the vacuum expectation value (vev) σ of a $SU(2)$ singlet scalar field S. Accordingly, the Yukawa interactions of the high energy Lagrangian read

$$-\mathcal{L}_Y = \frac{1}{2}\bar{N}_\alpha M_{N_\alpha} N_\alpha + \bar{F}_a M_{F_a} F_a + h_{ia}\bar{\ell}_i P_R F_a \Phi + \bar{N}_\alpha \left(\lambda_{\alpha a} + \lambda^{(5)}_{\alpha a}\gamma_5\right) F_a S. \quad (1)$$

We use Greek indices $\alpha, \beta \ldots = 1, 2, 3$ to label the heavy Majorana neutrinos, Latin indices $a, b \ldots = 1, 2, 3$ for the vectorlike messengers, and $i, j, k, \ldots$ for the lepton flavors e, μ, τ. Following reference [8)] we chose the simple $U(1)_X$ charge assignments $X(\ell_{L_i}, F_{L_a}, F_{R_a}) = +1$, $X(S) = -1$ and $X(N_\alpha, \Phi) = 0$. This assignment is sufficient to enforce the absence of $\bar{N}\ell\Phi$ terms, but clearly it does not constitute an attempt to reproduce the fermion mass pattern, and accordingly we will also avoid assigning specific charges to the right-handed leptons and quark fields that have no relevance for our analysis. As discussed in [8)], depending on the hierarchy between the relevant scales of the model

$(M_{N_1}, M_{F_a}, \sigma)$, quite different *scenarios* for leptogenesis can arise: *i)* For $M_F, \sigma \gg M_N$, we recover the Standard Leptogenesis (SL) case that will not discuss. *ii)* For $\sigma < M_{N_1} < M_{F_a}$ we obtain the Purely Flavored Leptogenesis (PFL) case, that corresponds to the situation, when the flavor symmetry $U(1)_X$ is still unbroken during the leptogenesis era and at the same time the messengers F_a are too heavy to be produced in N_1 decays and scatterings, and can be integrated away (for other possibilities see ref. 8)). After $U(1)_X$ and electroweak symmetry breaking the set of Yukawa interactions in (1) generates light neutrino masses through the effective mass operator. The resulting mass matrix can be written as 8)

$$-\mathcal{M}_{ij} = \left[h^* \frac{\sigma}{M_F} \lambda^T \frac{v^2}{M_N} \lambda \frac{\sigma}{M_F} h^\dagger\right]_{ij} = \left[\tilde{\lambda}^T \frac{v^2}{M_N} \tilde{\lambda}\right]_{ij} . \tag{2}$$

Here we have introduced the seesaw-like couplings $\tilde{\lambda}_{\alpha i} = \left(\lambda \frac{\sigma}{M_F} h^\dagger\right)_{\alpha i}$. Note that, in contrast to the standard seesaw, the neutrino mass matrix is of fourth order in the *fundamental* Yukawa couplings (h and λ) and due to the factor σ^2/M_F^2 is even more suppressed.

3 Purely flavored leptogenesis

In the case when $\sigma < M_{N_1} < M_F$, two-body N_1 decays are kinematically forbidden. However, via off-shell exchange of the heavy F_a fields, N_1 can decay to the three body final states $S\Phi l$ and $\bar{S}\bar{\Phi}\bar{l}$. The CP asymmetry is obtained from the interference between the tree level and loop diagrams; and reads 8):

$$\epsilon_{N_1 \to \ell_j} \equiv \epsilon_j = \frac{3}{128\pi} \frac{\sum_i \Im m \left[\left(h r^2 h^\dagger\right)_{ij} \tilde{\lambda}_{1i} \tilde{\lambda}^*_{1j}\right]}{\left(\tilde{\lambda}\tilde{\lambda}^\dagger\right)_{11}}, \tag{3}$$

where $r = M_{N_1}/M_F$. The CP asymmetries in (3) have the following properties: *i)* $\epsilon_j \neq 0$. *ii)* The total CP asymmetry $\epsilon_{N_1} = \sum_j \epsilon_j = 0$. This is because $\Im m[\tilde{\lambda} h r^2 h^\dagger \tilde{\lambda}^\dagger]_{11} = 0$, and is related to the fact that the loop does no involve lepton number violation. *iii)* Rescaling the couplings h and λ by a parameter $\kappa > 1$ according to: $h \to \kappa h$, $\lambda \to \kappa^{-1}\lambda$; enhances the CP asymmetries as $\epsilon_i \to \kappa^2 \epsilon_i$ 9). In the Bolztmann Equations (BE), the particles densities are written in terms of the entropy density s, i.e $Y_a = n_a/s$ where n_a is the number density for the particle a. We rescale the densities Y_a by the equilibrium density

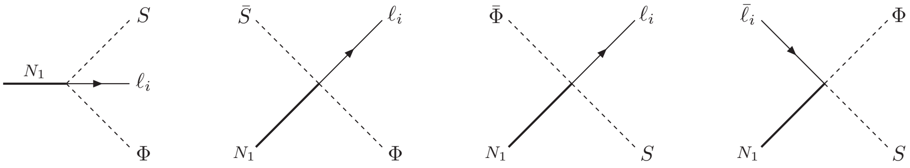

Figure 1: Relevant diagrams for leptogesis in our PFL model.

Y_a^{eq} of the corresponding particle, defining $y_a \equiv Y_a/Y_a^{eq}$, while the asymmetries of the rescaled densities are denoted by $\Delta y_a \equiv y_a - y_{\bar{a}}$. In the BE, the time derivative is defined as $\dot{Y}_a = zHs\frac{dY_a}{dz}$ where $z = M_{N_1}/T$ and $H(z)$ is the Hubble rate at temperature T. We denote the thermally averaged rate for an initial state A to go the final state B as $\gamma_B^A = \gamma\,(A \to B)$. The processes in the BE are the decay of N_1 and the scatterings illustrated in figure 1; they are all of the same order $\mathcal{O}((\lambda^\dagger h)^2)$. The BE for the evolution of the N_1 abundance and of the lepton density asymmetry $Y_{\Delta L_i}$ are (see 9) for details):

$$\begin{aligned} \dot{Y}_{N_1} &= -\,(y_{N_1}-1)\,\gamma \\ \dot{Y}_{\Delta L_i} &= (y_{N_1}-1)\,\epsilon_i\gamma - \Delta y_i\left(\gamma_i + (y_{N_1}-1)\,\gamma_{S\Phi}^{N_1\bar{\ell}_i}\right), \end{aligned} \tag{4}$$

where $\gamma_i = \gamma_{S\Phi\ell_i}^{N_1} + \gamma_{\Phi\ell_i}^{\bar{S}N_1} + \gamma_{S\ell_i}^{\bar{\Phi}N_1} + \gamma_{S\Phi}^{\bar{\ell}_iN_1}$ is the sum of the processes depicted en fig. 1 and $\gamma = \sum_i \gamma_i + \bar{\gamma}_i$. For PFL the strong washout condition, corresponds to: $\frac{\gamma}{z\,H\,s}\Big|_{z\sim1} > 1$ where the normalization factor $z\,H\,s$ has been chosen to obtain an adimensional ratio. For the BE's solution we have chosen the couplings h and λ such that they reproduce the low energy neutrino parameters within $2\,\sigma$ and also satisfy the strong washout condition. The densities rates for e and τ are shown in figure 2, their expressions can be found in 9). It is important to remark that the value of the lowest Majorana mass has be chosen at the TeV scale: $M_{N_1} = 2.5$ TeV. Others parameters are $M_{N_2} = 10$ TeV, $M_{N_3} = 15$ TeV and $r_a = [.1, .01, .001]$. The total reaction densities that determine the washout rates for the different flavors are shown in the first panel in figure 3. Since PFL is defined by the condition that the sum of the flavor CP asymmetry vanishes ($\sum_j \epsilon_{1j} = 0$), it is the hierarchy between these washout rates that in the end is the responsible for generating a net lepton number asymmetry. The total lepton asymmetry obtained is above the experimental data, but the couplings can be rescaled by a suitable value of κ to get the right value.

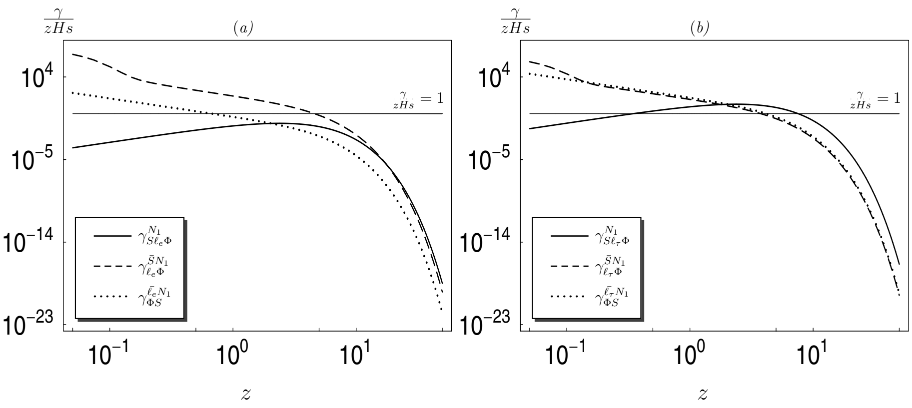

Figure 2: (a) The e density rates. Around $z \sim 1$ s-channel scatterings is the dominant one. (b) The τ density rates. Around $z \sim 1$ both decay and scatterings are faster than $z\,H\,s$.

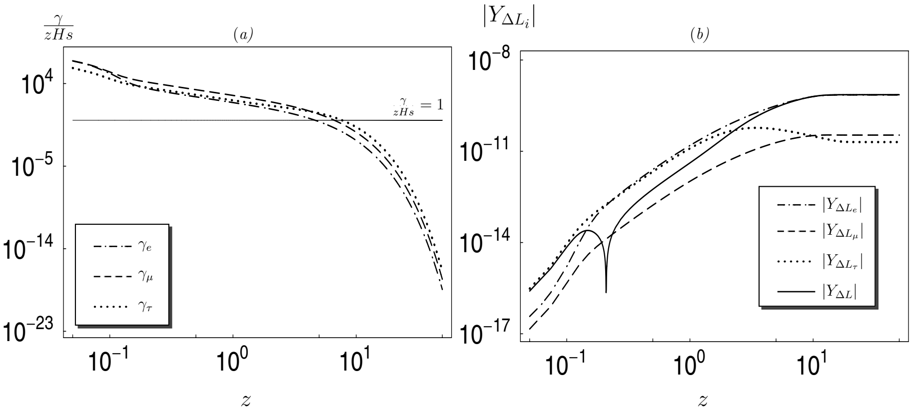

Figure 3: (a) Washout rates: with our choice of parameters the washout for the τ is stronger (weaker) than that of e and μ, for $z \gg 1$ ($z \ll 1$). (b) Evolution of the flavored and of the total lepton asymmetry. The final value is $Y_{\Delta L} = -7.1 \times 10^{-10}$, that is approximately three times larger than the experimental value, and is completely dominated by $Y_{\Delta L_e}$.

Conclusions

Variations of the standard leptogenesis scenario can arise from the presence of an additional energy scale different from that of lepton number violation.

Quite generically, the resulting scenarios can be expected to be qualitatively and quantitatively different from SL. Here we have considered what we regard as the simplest possibility namely, the presence of an Abelian flavor symmetry $U(1)_X$. The model allows for the possibility of generating the Cosmic baryon asymmetry at a scale of a few TeVs. Moreover, our analysis provides a concrete example of PFL, and shows that the condition $\epsilon_1 \neq 0$ is by no means required for successful leptogenesis.

References

1. G. Hinshaw *et al.* [WMAP Collaboration], Astrophys. J. Suppl. **180**, 225 (2009) [arXiv:0803.0732 [astro-ph]].
2. A. D. Sakharov, Pisma Zh. Eksp. Teor. Fiz. **5**, 32 (1967) [JETP Lett. **5**, 24 (1967 SOPUA,34,392-393.1991 UFNAA,161,61-64.1991)].
3. A. D. Dolgov, Phys. Rept. **222**, 309 (1992).
4. M. Fukugita and T. Yanagida, Phys. Lett. B **174**, 45 (1986).
5. V. A. Kuzmin, V. A. Rubakov and M. E. Shaposhnikov, Phys. Lett. B **155**, 36 (1985).
6. P. Minkowski, Phys. Lett. B **67**, 421 (1977).
7. S. Davidson, E. Nardi and Y. Nir, Phys. Rept. **466**, 105 (2008) [arXiv:0802.2962 [hep-ph]].
8. D. Aristizabal Sierra, M. Losada and E. Nardi, Phys. Lett. B **659**, 328 (2008) [arXiv:0705.1489 [hep-ph]].
9. D. A. Sierra, L. A. Munoz and E. Nardi, arXiv:0904.3043 [hep-ph].

Frascati Physics Series Vol. XLVIII (2009), pp. 19-24
Young Researchers Workshop: *"Physics Challenges in the LHC Era"*
Frascati, May 11 and 14, 2009

HADRONIC τ DECAYS INTO TWO AND THREE MESON MODES WITHIN RESONANCE CHIRAL THEORY

Pablo Roig
IFIC (CSIC-Universitat de València) and Physik Department (TUM-Munchen)

Abstract

We study two and three meson decays of the tau lepton within the framework of the Resonance Chiral Theory, that is based on the following properties of QCD: its chiral symmetry in the massless case, its large-N_C limit, and the asymptotic behaviour it demands to the relevant form factors.
Most of the couplings in the Lagrangian are determined this way rendering the theory predictive. Our outcomes can be tested thanks to the combination of a very good experimental effort (current and forthcoming, at B- and tau-charm-factories) and the very accurate devoted Monte Carlo generators.

1 Hadronic decays of the τ lepton

Our purpose is to provide a description of the semileptonic decays of the tau lepton that incorporates as many theoretical restrictions derived from the fundamental interaction, QCD 1), as possible. This is a very convenient scenario

to investigate the hadronization of QCD because one fermionic current is purely leptonic and thus calculable unambiguously so that we can concentrate our efforts on the other one, involving light quarks coupled to a $V-A$ current.
The decay amplitude for the considered decays may be written as:

$$\mathcal{M} \;=\; -\frac{G_F}{\sqrt{2}}\, V_{\mathrm{ud/us}}\, \overline{u}_{\nu_\tau}\gamma^\mu(1-\gamma_5)\, u_\tau \mathcal{H}_\mu \,, \tag{1}$$

where the strong interacting part is encoded in the hadronic vector, $\mathcal{H}_\mu$:

$$\mathcal{H}_\mu = \langle\, \{P(p_i)\}_{i=1}^n \,|\, (\mathcal{V}_\mu - \mathcal{A}_\mu)\, e^{i\mathcal{L}_{QCD}} |0\,\rangle\,. \tag{2}$$

Symmetries let us decompose $\mathcal{H}_\mu$ depending on the number of final-state pseudoscalar (P) mesons, n.
One meson tau decays can be predicted in terms of the measured processes $(\pi/K)^- \to \mu^-\nu_\mu$, since the matrix elements are related. This provides a precise test of charged current universality [2]. On the other side, it cannot tell anything new on hadronization.
The two-pion tau decay is conventionally parameterized -in the isospin limit, that we always assume- just in terms of the vector $(J^P = 1^-)$ form factor of the pion, $F_\pi(s)$:

$$\langle\, \pi^-\pi^0 | \bar{d}\gamma^\mu u | 0\,\rangle \equiv \langle\, \pi^-\pi^0 | V^\mu \mathrm{e}^{i\mathcal{L}_{QCD}} | 0\,\rangle \equiv \sqrt{2} F_\pi(s) (p_{\pi^-} - p_{\pi^0})^\mu \,, \tag{3}$$

where $s \equiv (p_{\pi^-} + p_{\pi^0})^2$.
Because $SU(3)$ is broken appreciably by the difference between m_s and $(m_u + m_d)/2$, two form factors are needed to describe the decays involving one pion and one kaon:

$$\begin{aligned}\langle\, \pi^-(p')\bar{K}^0(p) | V^\mu \mathrm{e}^{i\mathcal{L}_{QCD}} | 0\,\rangle \;\;\equiv\;\; & \left(\frac{Q^\mu Q^\nu}{Q^2} - g^{\mu\nu}\right)(p-p')_\nu F_+^{K\pi}(Q^2) \\ & - \frac{m_K^2 - m_\pi^2}{Q^2} Q^\mu F_0^{K\pi}(Q^2)\,,\end{aligned} \tag{4}$$

where $Q^\mu \equiv (p+p')^\mu$. $F_+^{K\pi}(Q^2)$ carries quantum numbers 1^-, while $F_0^{K\pi}(Q^2)$ is the pseudoscalar form factor (0^-). Other two meson decays can be treated similarly and one should take advantage of the fact that chiral symmetry relates some of their matrix elements.
For three mesons in the final state, the most general decomposition reads:

$$\begin{aligned}\mathcal{H}_\mu = & V_{1\mu} F_1^A(Q^2, s_1, s_2) + V_{2\mu} F_2^A(Q^2, s_1, s_2) + \\ & Q_\mu F_3^A(Q^2, s_1, s_2) + i\, V_{3\mu} F_4^V(Q^2, s_1, s_2)\,,\end{aligned} \tag{5}$$

and

$$
\begin{aligned}
V_{1\mu} &= \left(g_{\mu\nu} - \frac{Q_\mu Q_\nu}{Q^2} \right) (p_2 - p_1)^\nu, \;\; V_{2\mu} = \left(g_{\mu\nu} - \frac{Q_\mu Q_\nu}{Q^2} \right) (p_3 - p_1)^\nu \,, \\
V_{3\mu} &= \varepsilon_{\mu\nu\varrho\sigma}\, p_1^\nu \, p_2^\varrho \, p_3^\sigma, \;\; Q_\mu = (p_1 \, + \, p_2 \, + \, p_3)_\mu \,, \, s_i = (Q - p_i)^2 \,. \qquad (6)
\end{aligned}
$$

F_i, $i = 1, 2, 3$, correspond to the axial-vector current ($\mathcal{A}_\mu$) while F_4 drives the vector current ($\mathcal{V}_\mu$). The form factors F_1 and F_2 have a transverse structure in the total hadron momenta, Q^μ, and drive a $J^P = 1^+$ transition. The pseudoscalar form factor, F_3, vanishes as m_P^2/Q^2 and, accordingly, gives a tiny contribution. Higher-multiplicity modes can be described proceeding similarly 3). This is as far as we can go without model assumptions, that is, it is not yet known how to obtain the F_i from QCD. However, one can derive some of their properties from the underlying theory, as we will explain in the following.

2 Theoretical framework: Resonance Chiral Theory

We use a phenomenological Lagrangian 4) written in terms of the relevant degrees of freedom that become active through the energy interval spanned by hadronic tau decays. The chiral symmetry of massless QCD determines 5) the chiral invariant operators that can be written including the lightest mesons in the spectrum, the pseudoscalar ones belonging to the pion multiplet. It was carefully checked 6) that -as one expects- Chiral Perturbation Theory, χPT, can only describe a little very-low-energy part of semileptonic tau decays.
Then one may attempt to extend the range of applicability of χPT to higher energies while keeping its predictions for the form factors at low momentum: this is the purpose of Resonance Chiral Theory, $R\chi T$, 7) that includes the light-flavoured resonances as explicit fields in the action.
At LO in the $N_C \to \infty$ limit of QCD 8) one has as infinite tower of stable mesons that experience local effective interactions at tree level. We depart from this picture in two ways:

- We incorporate the widths of the resonances worked out consistently within $R\chi T$ 9).
- We attempt a description including the least possible number of resonance fields reducing -ideally- to the single resonance approximation, SRA 10).

We take vector meson dominance into account when writing our Lagrangian. Thus, it will consist of terms accounting for the following interactions (a_μ, v_μ stand for the axial(-vector) currents and A and V for the axial(-vector) resonances):

- Those in χPT at LO and χPT-like: $a_\mu P$, $a_\mu PPP$, $PPPP$ with even-intrinsic parity; and $v_\mu PPP$ in the odd-intrinsic parity sector.
- Those relevant in $R\chi T$ -NLO χPT operators are not included to avoid double counting, since they are recovered and their couplings are saturated upon integration of the resonance contributions 7)-. They include: $a_\mu VP$, $v_\mu V$, $a_\mu A$, VPP and AVP in the even-intrinsic parity sector and $v_\mu VP$, $VPPP$ and VVP in the odd-parity one.

The explicit form of the operators and the naming for the couplings can be read from 7), 11), 12), 13), 14) and 15).

The $R\chi T$ just determined by symmetries does not share the UV QCD behaviour yet. For this, and for our purposes, we need to impose appropriate Brodsky-Lepage conditions 16) on the relevant form factors. Explicit computation and these short-distance restrictions reduce appreciably the number of independent couplings entering the amplitudes which enables us to end up with a useful -that is, predictive- theory.

3 Phenomenology

Our framework describes pretty well the two-meson decays of the τ, as shown in the $\pi\pi$ 17) and $K\pi$ 18) cases. Two-meson modes including η can be worked analogously. The data in these modes are so precise [1] that although the SRA describes the gross features of the data, one needs to include the first excitations of the V resonances to achieve an accurate description. Although $F_+^{K\pi}(Q^2)$ is much more important than $F_0^{K\pi}(Q^2)$, one needs an appropriate pseudoscalar form factor to fit well the data, specially close to threshold 18).
The three meson modes are much more involved. However, a good description of the data has been achieved through a careful study 12, 15) taking into account all theory constrains and experimental data on the 3π and $KK\pi$ channels. We predict the $KK\pi$ spectral function and conclude that the vector

---

[1] See the references quoted in the articles cited through the section.

current contribution cannot be neglected in these modes. We will study the other three meson modes along the same lines. In particular, our study of the $K\pi\pi$ channels might help improve the simultaneous extraction of m_s and V_{us} 19). Our expressions for the vector and axial-vector widths and the hadronic matrix elements have been implemented successfully in the TAUOLA library 20). This way, the experimental comunity will have as its disposal a way of analysing hadronic decays of the tau that includes as much as possible information from the fundamental theory. We also plan to study $e^+e^- \to PPP$ at low energies what can eventually be used by 21).

4 Acknowledgements

I congratulate the local organizing committee for this first edition of the Young Researchers Workshop as well as for the XIV LNF SPRING SCHOOL BRUNO TOUSCHEK held in parallel. I am grateful to Jorge Portolés for a careful revision and useful suggestions on the draft. I acknowledge useful discussions with Olga Shekhovtsova. This work has been supported in part by the EU MRTN-CT-2006-035482 (FLAVIAnet) and by the DFG cluster of excellence 'Origin and structure of the Universe' .

References

1. H. Fritzsch, M. Gell-Mann and H. Leutwyler, Phys. Lett. B **47** (1973) 365. D. J. Gross and F. Wilczek, Phys. Rev. Lett. **30** (1973) 1343. H. D. Politzer, Phys. Rev. Lett. **30** (1973) 1346.

2. A. Pich, Nucl. Phys. Proc. Suppl. **98** (2001) 385. Nucl. Phys. Proc. Suppl. **181-182** (2008) 300.

3. R. Fischer, J. Wess and F. Wagner, Z. Phys. C **3** (1979) 313.

4. S. Weinberg, Physica A **96** (1979) 327.

5. J. Gasser and H. Leutwyler, Annals Phys. **158** (1984) 142. Nucl. Phys. B **250** (1985) 465.

6. G. Colangelo, M. Finkemeier and R. Urech, Phys. Rev. D **54** (1996) 4403.

7. G. Ecker, J. Gasser, A. Pich and E. de Rafael, Nucl. Phys. B **321** (1989) 311. G. Ecker, J. Gasser, H. Leutwyler, A. Pich and E. de Rafael, Phys. Lett. B **223** (1989) 425.

8. G. 't Hooft, Nucl. Phys. B **72** (1974) 461, **75** (1974) 461. E. Witten, Nucl. Phys. B **160** (1979) 57.

9. D. Gómez Dumm, A. Pich and J. Portolés, Phys. Rev. D **62** (2000) 054014.

10. M. Knecht, S. Peris, M. Perrottet and E. de Rafael, Phys. Rev. Lett. **83** (1999) 5230.

11. P. D. Ruiz-Femenía, A. Pich and J. Portolés, JHEP **0307** (2003) 003.

12. D. Gómez Dumm, A. Pich and J. Portolés, Phys. Rev. D **69** (2004) 073002.

13. V. Cirigliano, G. Ecker, M. Eidemüller, A. Pich and J. Portolés, Phys. Lett. B **596** (2004) 96.

14. P. Roig, AIP Conf. Proc. **964** (2007) 40.

15. D. Gómez-Dumm, P. Roig, A. Pich, J. Portolés, to appear.

16. S. J. Brodsky and G. R. Farrar, Phys. Rev. Lett. **31** (1973) 1153. G. P. Lepage and S. J. Brodsky, Phys. Rev. D **22** (1980) 2157.

17. F. Guerrero and A. Pich, Phys. Lett. B **412** (1997) 382. A. Pich and J. Portolés, Phys. Rev. D **63** (2001) 093005. Nucl. Phys. Proc. Suppl. **121** (2003) 179.

18. M. Jamin, A. Pich and J. Portolés, Phys. Lett. B **640** (2006) 176 Phys. Lett. B **664** (2008) 78.

19. E. Gámiz, M. Jamin, A. Pich, J. Prades and F. Schwab, Phys. Rev. Lett. **94** (2005) 011803.

20. O.Shekhovtsova, private communication.

21. G. Rodrigo, H. Czyz, J. H. Kühn and M. Szopa, Eur. Phys. J. C **24** (2002) 71.

Frascati Physics Series Vol. XLVIII (2009), pp. 25-30
YOUNG RESEARCHERS WORKSHOP: *"Physics Challenges in the LHC Era"*
Frascati, May 11 and 14, 2009

MEASUREMENT OF THE MISSING TRANSVERSE ENERGY IN THE ATLAS DETECTOR

Giovanni Siragusa
Johannes Gutenberg Universität - Mainz (DE)

Abstract

A very good measurement of the Missing Transverse Energy (E_T^{miss}) is a crucial requirement for the study of many physics processes at the LHC, for example the Standard Model W or top-quark production, Higgs bosons decaying to tau pairs, or supersymmetric particles. The most important contribution to the E_T^{miss} resolution in the ATLAS detector comes from the calorimeters, which provide near hermetic energy reconstruction. The calorimeter noise suppression is of crucial importance and can be achieved using either a simple noise cut or more sophisticated topological criteria. A refined calibration improves the E_T^{miss} measurement. Additional corrections are applied for muons detected in the Muon Spectrometer and energy deposits in dead material, as the cryostat of the calorimeter. A detailed study of the Missing Energy performance on fully simulated Monte Carlo data is presented, which shows results for various physics processes involving different level of hadronic activity and E_T^{miss}. Real ATLAS data from cosmic runs are also compared with the results from the detector simulation.

1 Introduction

At Tevatron and at the Large Hadron Collider (LHC) events with large Transverse Missing Energy (E_T^{miss}) are expected to be key signatures of new physics (SUSY, Extra Dimensions). A good measurement of E_T^{miss} in terms of linearity and resolution is important for the reconstruction of the top-quark mass and for the study of W bosons decays. A precise E_T^{miss} measurement is also crucial for the efficient and accurate reconstruction of the Higgs boson mass, when decaying to a pair of τ leptons.

At hadron colliders it is not possible to use the Centre of Mass Energy to constrain the kinematic of observed decays, but only the conservation of the longitudinal momentum. To reconstruct the transverse momentum (p$_T$) of non interacting particles we make use of the conservation of the total longitudinal momentum of the event: $\overrightarrow{E_T}^{miss} = -\overrightarrow{E_T}^{visible}$. For this reason the LHC general purpose detectors have been designed with calorimeters covering a large solid angle. In particular, the ATLAS calorimeter is able to provide a precise energy measurement up to a pseudo-rapidity of $|\eta| < 4.9$.

To properly reconstruct the visible energy of the event, each energy deposit has to be calibrated accordingly to the associated physics process. One of the challenges of the measurement is to calibrate the energy deposited by soft interactions, which contribute significantly to the total visible energy of the event. The main sources of soft deposits are inelastic proton-proton collisions (pile-up) and the underlying event. The limited coverage of the ATLAS Inner Detector and of the Muon Spectrometer, and the cracks of the Calorimeters in the barrel-endcap transition region affect the E_T^{miss} measurement.

2 E_T^{miss} reconstruction

To measure E_T^{miss} in ATLAS two approaches are used: the first (that we will denote as *cell-based reconstruction*) starts from the calorimeter cells and adds calibration and corrections in further steps, the second (that we will denote as *object-based reconstruction*) starts from identified objects and adds the contribution from soft deposits in a second step. The cell-based reconstruction is more robust at initial data-taking, and less dependent on the definition of each single physics object. The object based reconstruction, on the other side, has the advantage to treat separately low-energy deposits: isolated clusters are collected in the so called *mini jets*, then $\pi^{\pm}$ and π^{0} are identified and calibrated. Given the high number of electronic channels in the calorimeters ($\sim 200\ k$), an efficient noise suppression is required to improve the resolution. The easiest approach consists in a determination of the electronic noise, which is then used to apply a cut on each calorimeter cell energy, usually requiring $E_{cell} > 2 \times \sigma_{noise}$. A more effective approach, while less conservative, is the *Topological Clustering*, with the search for three-dimensional clusters of cells. Starting from a cluster seed (a cell with an energy above $4 \times \sigma_{noise}$), all the neighbouring cells with energy above $2 \times \sigma_{noise}$ are added to the cluster, then all their neighbouring cells without requiring any energy cut. With this method cells with very low signal can survive the noise cut because of a signal measured in a neighbouring cell. In Fig.(1, left) the E_T^{miss} distribution is shown for randomly triggered events in cosmic data taking, after applying both noise suppression methods. It's observed that the Topological Clustering improves the measurement, considering that the expected E_T^{miss} in randomly triggered events is zero. In Fig.(1, right) the cosmic data are also compared with the results obtained with the full Monte Carlo simulation of the ATLAS detector.

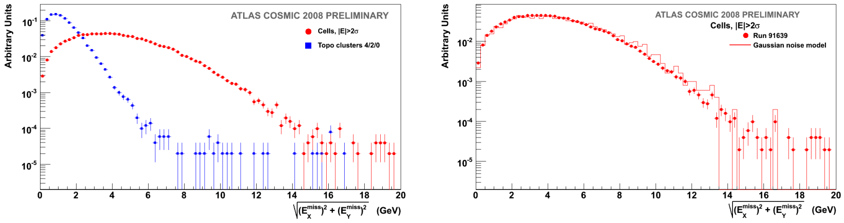

Figure 1: *Left)* E_T^{miss} *in cosmic data from random triggers for standard noise suppression and topological clustering. Right) Comparison between* E_T^{miss} *in full detector simulation (line) and cosmic data (dots).*

In the Cell-based reconstruction, the calibrations are applied in two main steps. Firstly the *global calibration*, which is based on the characteristics of the energy deposits, like the energy density or the spatial shape of the signal. In a second step, the *refined calibration* is applied to all reconstructed objects, preventing overlaps (if a cell is associated to a physical object it can not be associated to another one). The Object-based reconstruction, on the other hand, starts from calibrated objects and then performs a further calibration of the soft energy deposits (using the classification in $\pi^{\pm}$ and π^0). In Fig.(2, left) the *Linearity*[1] is shown for different physics processes. It is possible to observe how the calibration improves the linearity, which is at % level. Processes with lower levels of hadronic activity (e.g. $W \rightarrow e\nu$ and $W \rightarrow \mu\nu$) are characterized by a good resolution already at the electro-magnetic scale. In Fig.(2, right) the Missing E_T resolution is also shown for the Higgs$\rightarrow \tau\tau$ decay as a function of the Truth Missing E_T of the event. At low Missing E_T the resolution is worsened because the noise becomes dominant.

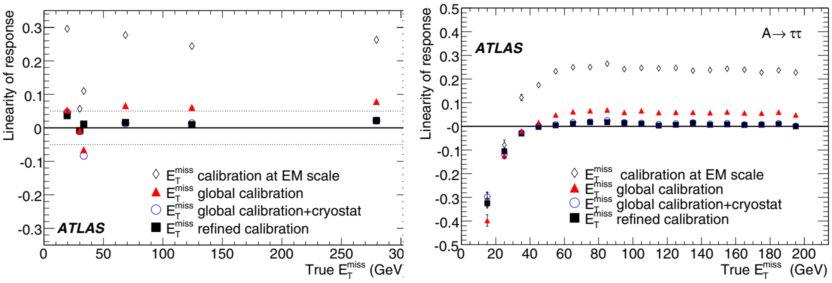

Figure 2: *Left) E_T^{miss} linearity for different processes and different levels of calibration. In order of increasing Truth $< E_T^{miss} >$: $Z \rightarrow \tau\tau$, $W \rightarrow e\nu$, $W \rightarrow \mu\nu$, semi-leptonic $t\bar{t}$, Higgs$\rightarrow \tau\tau$, SUSY particle at a mass of ~ 1 TeV. Right) E_T^{miss} linearity as a function of the Truth E_T^{miss} for $A \rightarrow \tau\tau$.*

3 E_T^{miss} performance

The E_T^{miss} performance has been studied using fully simulated Monte Carlo data. The results shown here have been obtained in the context of the *Computing System Commissioning* of the ATLAS experiment.

The E_T^{miss} resolution follows approximately a stochastic behaviour as a function of the total transverse energy of the event ($\sum E_T$). It can be measured

---

[1] The Linearity is defined as the relative difference between reconstructed and truth Missing E_T: $({E_T^{miss}}_{Reco} - {E_T^{miss}}_{Truth})/{E_T^{miss}}_{Truth}$, where truth and reconstruced E_T^{miss} are obtained as the mean value of a Gaussian fit to the E_T^{miss} distribution.

in-situ using known processes with zero expected E_T^{miss}, like minimum bias events which have also a very large cross-section. In Fig.(3, left) the E_T^{miss} resolution is shown for minimum bias and di-jet events, where only the minimum bias events are used for the fit. It's possible to observe how well the resolution is described up to high values of the total transverse energy. In Fig.(3, right) the Missing E_T resolution is shown for different physics processes. Deviation from the expected shape (a square root, as fitted in figure) can be observed at low and at high $\sum E_T$: at low $\sum E_T$ the noise starts to play an important role, while at high $\sum E_T$ the constant term of the calorimeter resolution dominates over the other contributions.

The limited acceptance of the Muon Spectrometer affects the measurement because there might be undetected muons which can contribute to the fake Missing E_T. Also the jet measurement requires some care, since the jets can deposit energy in poorly instrumented regions of the calorimeters. The calorimeter leakage can be improved using informations from the Inner Tracker, while for the muons we can rely only on statistical estimation of the fake contribution.

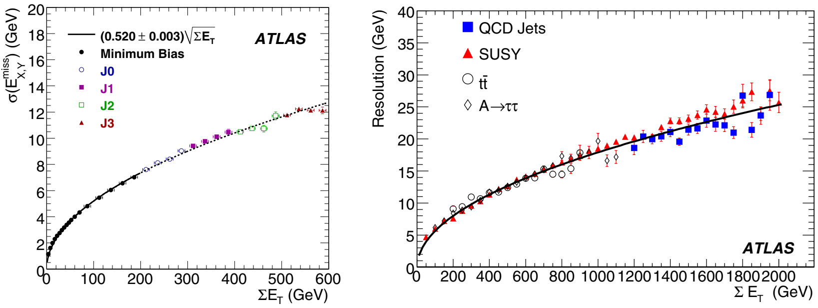

Figure 3: *Left)* $E_{x,y}^{miss}$ *resolution for minimum-bias and di-jet events. The fit is done using only the minimum bias events. Right)* $E_{x,y}^{miss}$ *resolution for various interesting physics processes.*

To properly calibrate the Missing E_T in ATLAS, various interesting physics processes have been identified. Furthermore the Missing E_T performance is strictly related to the jet calibration. As already mentioned, the high statistics of minimum bias events that will be available already at low luminosity will be very useful for understanding the QCD environment at the LHC energies. Di-jet events are as much powerful as minimum bias and, despite that of a lower statistics, they present higher values of $\sum E_T$. Other processes that are useful for the understanding of the Missing E_T are $Z \rightarrow e^+e^-$ and $Z \rightarrow \mu^+\mu^-$, which acn give interesting results in terms of resolution and acceptance, while $Z \rightarrow \tau^+\tau^-$ can be used to fix the E_T^{miss} scale.

4 Conclusion

The main aspects of the Missing E_T reconstruction and performance in ATLAS have been shown. Detailed MC studies demonstrate that the expected performance can be achieved, while runs with random triggers have demonstrated that the description and suppression of the instrumental noise work well. In view of first collision data, further studies of the cosmic data will improve our understanding of the Missing E_T.

References

1. The ATLAS Collaboration, "Expected performance of the ATLAS Experiment: Detector, Trigger and Physics", arXiv:0901.0512; CERN-OPEN-2008-20 (December 2008).

Frascati Physics Series Vol. XLVIII (2009), pp. 31-36
YOUNG RESEARCHERS WORKSHOP: *"Physics Challenges in the LHC Era"*
Frascati, May 11 and 14, 2009

MEASUREMENT OF THE pp→ Z→ $\mu\mu + X$ CROSS SECTION AT LHC WITH ATLAS EXPERIMENT

Roberto Di Nardo
INFN & University of Rome "Tor Vergata"
Via della Ricerca Scientifica 1, 00133 Rome

Abstract

One of the first Standard Model processes that can be studied with the ATLAS detector at the Large Hadron Collider will be the Z boson production in proton proton collisions. Due to its high production rate, the differents decay channels of the Z boson will also be used in the initial data taking period as benchmark processes for the calibration of the detectors and performance measurements. The measurement of the cross section of pp→Z→ $\mu^+\mu^- + X$ process with first data in ATLAS experiment is discussed.

1 Introduction

Due to large production rates, the physics of W and Z bosons is accessible in the early data taking phase of the ATLAS 1) experiment at the LHC and will be used as *standard candle* for many measurements. Depending on integrated luminosity, their leptonic decay channels can be used for the commissioning of detectors and debugging of the analysis tools or the precision measurement of electroweak parameters.

The production cross section of the Z boson can be written as

$$\sigma_Z = \frac{N - B}{A \times \varepsilon \times \int L dt} \tag{1}$$

where N is the number of selected candidate events, B is the number of background events, A is the detector acceptance computed from MC studies, L is the luminosity and ε includes the reconstruction and trigger efficiency and the signal selection cut efficiency.

The measurement uncertainty gets contribution from different terms as follows

$$\frac{\delta\sigma}{\sigma} = \frac{\delta N \oplus \delta B}{N - B} \oplus \frac{\delta \mathscr{L}}{\mathscr{L}} \oplus \frac{\delta A}{A} \oplus \frac{\delta\epsilon}{\epsilon} \tag{2}$$

The term δN has a pure statistic origin and the relative error will decrease with increasing integrated luminosity $\mathscr{L}$, following the relation $\delta N/N \sim 1/\sqrt{\mathscr{L}}$. The other terms are δB due to background contribution, δA that reflects the theoretical uncertainties on the acceptance and $\delta\epsilon$ that is related to the limited detector response knowledge. All of these are systematic uncertainties in the cross section measurement but they can be constrained with auxiliary measurements. An overall luminosity uncertainty of $\delta\mathscr{L}/\mathscr{L} = 10\%$ should be taken into account for the measurement with the first $\sim 50\text{pb}^{-1}$ of integrated luminosity, but it is expected to decrease in time thanks to the better understanding of the LHC beam parameters and of the ATLAS luminosity detector response.

In the following sections, the measurement of $\sigma\left(pp \rightarrow Z\right) \times BR\left(Z \rightarrow \mu\mu\right)$ is discussed. Section 2 will focus on the event selection while in the other chapter the techniques for the determination of the detector performance from data are shortly described: the muon momentum scale and resolution (section 3) and the measurement of muon reconstruction and trigger efficiency (section 4).

2 Event Selection

The $Z \rightarrow \mu^+\mu^-$ signal selection begins requiring at least a muon track candidate that passes the 10 GeV single muon trigger. Events are further selected by requiring that they contain at least two reconstructed muon tracks with a

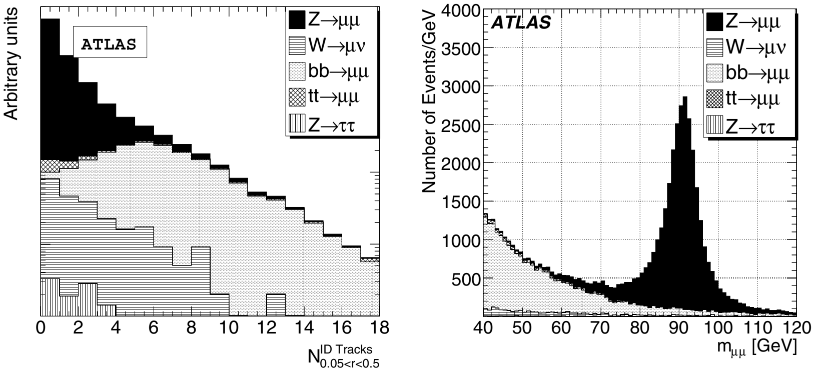

(a) (b)

Figure 1: *a) Distribution of the track multiplicity within* $\Delta R = 0.5$ *around the muon b) Di-muon invariant mass distribution for* $Z \to \mu^+\mu^-$ *signal and background after all cuts, except the isolation and* $M_{\mu\mu}$ *cuts, for 50* pb^{-1}.

transverse momentum $p_T > 20$ GeV and $|\eta| < 2.5$. The candidates must have an opposite charge, and the invariant mass of the muon pair $M_{\mu\mu}$ should fulfill $|91.2\text{GeV} - M_{\mu\mu}| < 20$ GeV. An isolation cut is also applied: the number of the tracks N^{ID} in the Inner Detector within a cone around the candidate muon with a size $\Delta R = \sqrt{\Delta\phi^2 + \Delta\eta^2} < 0.5$ must satisfy the relation $N^{ID} \leq 5$ and the sum of the transverse momentum of the tracks inside the same cone must not exceed 5 GeV. This is necessary to exclude non-isolated muons coming from jet events. Figure 1(a) $^{2)}$ shows the distribution of the track multiplicity, normalized to respective cross sections, for signal and background after all the other cuts.

These criteria select about 70% of the $Z \to \mu^+\mu^-$ events generated in the ATLAS detector acceptance that corresponds to $(2.57 \pm 0.02(stat)) \times 10^4$ signal events for an integrated luminosity of 50 pb^{-1} (at $\sqrt{s} = 14$ TeV); the residual background fraction is 0.004 ± 0.001. Figure 1(b) shows the resulting di-muon invariant mass for signal and background after all cuts, except the isolation and mass cuts, for an amount of data of 50 pb^{-1}.

3 Muon Momentum Scale and Resolution

The measurement of the muon momentum with the ATLAS experiment can be affected by the limited knowledge of the magnetic field, the uncertainty in the energy loss of the muons, and the alignment of the muon spectrometer.
The determination of the p_T scale and resolution one can be made studying the Z resonance shape. In fact the p_T scale has a direct impact on the measured mean value, while the p_T resolution has a direct impact on the measured Z width.
To extract the value of muon resolution and momentum scale, the p_T resolution function predicted by Monte Carlo simulations is iteratively adjusted in its width and scale and the corresponding Z boson mass distribution is calculated. The procedure stops if the resulting distribution agrees within its statistical error to the distribution measured from data.
It is expected to determine the momentum scale for muons with a precision better than 1%, while the uncertainty on the resolution will be smaller than 10%, for an integrated luminosity of $50\,\mathrm{pb}^{-1}$.

4 Muon Trigger and Reconstruction Efficiency

One of the methods chosen by the ATLAS experiment to evaluate the trigger and reconstruction efficiency for muons is the so called *tag and probe*. This is a data driven method which uses the two ATLAS independent traking systems (Muon Spectrometer and Inner Detector) to cross-check their performances.
The *tag and probe* method is based on the definition of a *probe* object that is used to make the performance measurement over a certain sample of events properly chosen (tagged). For the efficiency studies the *probe* assumes the same role of a MC truth generated muon in simulted data. In particular, the $Z \rightarrow \mu^+\mu^-$ decay provides two muons with an high p_T that can give two tracks in the Muon Spectrometer and in the Inner Detector and two combined objects.
To apply this method in the $Z \rightarrow \mu^+\mu^-$ decay, two reconstructed tracks in the Inner detector are required together with at least one associated track in the muon spectrometer. The invariant mass of the two Inner Detector tracks have to be close to the mass of the Z boson, to ensure that the tracks are the ones associated to the decay muons of the Z boson.
In order to get as close as possible to a zero-background sample (where this

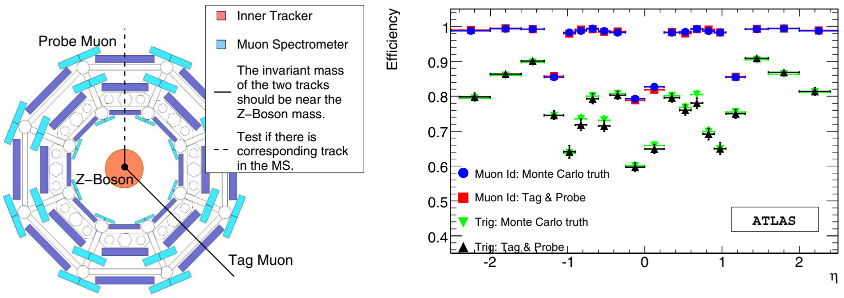

(a) (b)

Figure 2: *a) Schematic illustration of the tag and probe method. b) Muon detection efficiency vs. η, as measured from the tag-and-probe method and compared to the truth, for 50 pb^{-1}. The* 20 *GeV single muon trigger efficiency and the combined muon reconstruction efficiency are plotted.*

method for the efficiency estimation is exact) a tight trigger and quality cuts for the tag can be used. Figure 2(b) illustrate the 20 GeV single muon trigger efficiency and combined muon reconstruction efficiency using the tag and probe method compared to the MC truth.

5 Conclusion

In Table 1 the expected precision on the $\sigma\,(pp \to Z) \times BR\,(Z \to \mu\mu)$ measurement for an integrated luminosity of 50 pb^{-1} at $\sqrt{s} = 14$ TeV is shown.
With this amount of data, the signal and background acceptance uncertainties contribute to the cross section measurement error at the level of 2.3%, neglecting the uncertainty on the integrated luminosity. Except for the con-

Table 1: *Expected results for the $Z \to \mu^+\mu^-$ cross-section measurement with an integrated luminosity of* $50\,pb^{-1}$ *at* $\sqrt{s} = 14\,TeV$.

N ($\times 10^4$)	B ($\times 10^4$)	$A \times \epsilon$	$\delta A/A$	$\delta\epsilon/\epsilon$	σ(pb) $\pm\,(stat) \pm (sys)$
2.57 ± 0.02	0.010 ± 0.002	0.254	0.023	0.03	$2016 \pm 16 \pm 76$

tribution from the acceptance, which is theoretically limited, all the others uncertainties are expected to scale with statistics.
With the collection of a higher statistics, further studies of the differential $Z \rightarrow \mu^+\mu^-$ cross section will also be useful to improve the theoretical understanding, thus allowing to measure the $\sigma\,(pp \rightarrow Z) \times BR\,(Z \rightarrow \mu\mu)$ with a precision better than 2%.

References

1. The ATLAS Collaboration, The ATLAS Experiment at the CERN Large Hadron Collider, 2008 JINST 3 S08003

2. ATLAS Collaboration, Expected Performance of the ATLAS Experiment, Detector, Trigger and Physics, CERN-OPEN-2008-020, Geneva, 2008.

Frascati Physics Series Vol. XLVIII (2009), pp. 37-42
Young Researchers Workshop: *"Physics Challenges in the LHC Era"*
Frascati, May 11 and 14, 2009

STUDY OF THE GEOMETRICAL ACCEPTANCE FOR VECTOR BOSONS IN ATLAS AND ITS SYSTEMATIC UNCERTAINTY

Manuela Venturi
INFN and University of Roma Tor Vergata,
Via della Ricerca Scientifica 1, 00133 Rome, Italy

Abstract

The geometrical acceptance for the decays $pp \to W/Z + X \to \ell\nu/\ell^+\ell^- + X$ in the ATLAS detector, is calculated using different Monte Carlo generators. The main contribution to its systematic error is due to Parton Distribution Functions (PDFs).

1 Introduction

The measurement of $pp \to W/Z \to \ell\nu/\ell^+\ell^-$ cross sections will be one of the first goals of the ATLAS experiment when the LHC will start the first collisions in Winter 2009.

The cross section can be written as follows 1):

$$\sigma \equiv \sigma_{pp\to W/Z} \cdot \mathrm{Br}_{W/Z\to\ell\nu/\ell^+\ell^-} = \frac{N-B}{A\cdot\varepsilon\cdot\mathcal{L}} \qquad (1)$$

where Br is the branching ratio for the leptonic decays of vector bosons, N the number of signal events, B the number of associated background events, A the geometrical acceptance (i.e. the fraction of signal events inside the kinematical and angular cuts), ε the efficiency inside A and $\mathcal{L}$ the integrated luminosity. The geometrical acceptance is determined only by the theory: one generates the signal and looks for the final leptons, coming from the vector boson, and then imposes the best cuts in order to separate the signal from the background.

From eq.1 and assuming no correlation, we get the following formula to calculate cross section uncertainty 1):

$$\frac{\delta\sigma}{\sigma} = \frac{\delta N \oplus \delta B}{N - B} \oplus \frac{\delta\varepsilon}{\varepsilon} \oplus \frac{\delta\mathcal{L}}{\mathcal{L}} \oplus \frac{\delta A}{A} \tag{2}$$

where $\oplus$ means quadratic sum. $\delta N/\mathrm{N}$ and $\delta B/B$ have a purely statistical origin, so they will decrease as $1/\sqrt{\mathcal{L}}$, while $\delta\mathcal{L}$ and $\delta\varepsilon$ are expected to decrease thanks to detector understanding. As it is shown in tab.1, where an estimation for $pp \to Z \to e^+e^-$ is given, after an integrated luminosity of 1 fb^{-1} the main contribution to $\delta\sigma/\sigma$ will be the theoretical one, which is due to δA.

Table 1: *Estimated contributions for* $pp \to Z \to e^+e^-$ *cross section uncertainty versus integrated luminosity* 1)*.*

$\mathcal{L}$	$\delta\sigma/\sigma$ (stat)	$\delta\sigma/\sigma$ (sys)	$\delta\sigma/\sigma$ (lum)
50 pb^{-1}	0.8 %	4.1 %	10 %
1 fb^{-1}	0.2 %	2.4 %	–

2 Monte Carlo simulations of geometrical acceptance

I have compared acceptances calculated with different Monte Carlo generators: the *general purpose* `Herwig` 6.510 2) and `Pythia` 8.1 3) at Leading Order (LO) in α_s, and `Mc@Nlo` 3.3 4) at Next to Leading Order (NLO). Also `Horace` 3.2 5) has been used, both at LO and at NLO in α_{EW}, to quantify the impact of electroweak corrections.

In fact, different Monte Carlo generators implement different theoretical models, different parton shower approximations and different sensitive parameters, so it is important to compare results obtained with several generators.

In this work, the channels $\ell = e, \mu$ have been studied, both for W and for Z/γ^*, at $\sqrt{s} = 14$ TeV, in stand-alone mode and in the official ATLAS analysis framework (Athena).

For the muonic channel, to which tab.2 refers, the following cuts have been imposed on the final leptons:

- $p_T > 20\,\text{GeV}$ for μ and ν_μ,
- $|\eta| < 2.5$, only for μ.

Table 2: *Results for geometrical acceptance absolute values.*

	$W^+ \to \mu^+\nu_\mu$	$W^- \to \mu^-\overline{\nu}_\mu$	$Z \to \mu^+\mu^-$
`Herwig`	45.45 ± 0.30		39.98 ± 0.26
`Pythia`	45.99 ± 0.31		39.75 ± 0.26
`Horace` Born	45.82 ± 0.30	46.01 ± 0.31	38.93 ± 0.25
`Horace` NLO	47.87 ± 0.32	47.61 ± 0.32	42.01 ± 0.28
`Mc@Nlo`	48.31 ± 0.34	48.28 ± 0.34	42.62 ± 0.29

These values were obtained with small samples (about 40000 events/channel/generator), so the statistical binomial errors are quite large. Nevertheless, results appear in good agreement, as confirmed by the comparison among several distributions (leptons p_T and $|\eta|$, W and Z p_T and y). It is interesting to notice that both QCD (`Mc@Nlo`) and EW (`Horace`) corrections give an upward shift to the LO acceptance.

3 Acceptance uncertainty

As stated in the Introduction, the acceptance uncertainty will be the main contribution to that of cross section, setting the ultimate reachable accuracy.

The systematic error is studied starting from the `Mc@Nlo` *default configuration*, defined as “the most physical one”, and then turning on and off each effect indipendently to see the impact on A. The main contribution to $\delta A/A$ is due to PDFs uncertainty, while all the others (partonic intrinsic $k_T \neq 0$, initial state radiation amount, electromagnetic corrections, etc.) are negligible 6).

3.1 Parton Distribution Functions

Several analysis methods have been proposed to extract PDFs from data. To estimate $\delta A/A$, I compared the CTEQ and the Neural Network (NN) approaches.

3.1.1 CTEQ PDFs

CTEQ analysis implements the Hessian method: one chooses a priori the PDF parametrization ($N_{\mathrm{PAR}} = 20$ free parameters for CTEQ 6.1 analysis), and then iteratively diagonalizes the Hessian matrix, resulting in N_{PAR} eigenvectors. The last step requires to choose a *tolerance criterion* to stop the χ^2_{global} variation from the minimum, along each eigenvector. In this way, one ends up with $2N_{\mathrm{PAR}}$ PDF error sets plus a best fit set.

Acceptance central value, A_0, is calculated with the PDF best fit set, and then the Hessian error is associated to it through the master formula, which takes into account the possibility of an asymmetric behaviour:

$$\left.\begin{array}{l} \Delta A^{+} = \sqrt{\sum_{k=1}^{\mathrm{PAR}} \left[\max\left(A_k^{+} - A_0, A_k^{-} - A_0, 0\right)\right]^2} \\ \Delta A^{-} = \sqrt{\sum_{k=1}^{\mathrm{PAR}} \left[\max\left(A_0 - A_k^{+}, A_0 - A_k^{-}, 0\right)\right]^2} \end{array}\right. . \tag{3}$$

This is done with CTEQ 6, 6.1 and 6.6. While CTEQ 6.1 7) represent the improved version of 6, CTEQ 6.6 8) include heavy quark mass effects, in the General Mass VFN scheme. Moreover, CTEQ 6.6 analysis adds two degrees of freedom to the strange quark fit, shifting N_{PAR} from 20 to 22. Fig.1 shows this comparison for $W^{+} \to \mu^{+}\nu_{\mu}$.

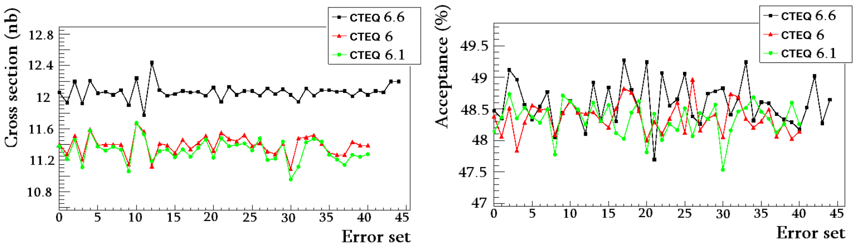

(a) (b)

Figure 1: *a) Cross sections and b) acceptances for* $pp \to W^{+} \to \mu^{+}\nu_{\mu}$.

Theoretical cross sections (fig.1(a)) increase up to $\sim 6\%$, while for acceptances (fig.1(b)) no conclusion can be drawn yet, due to small statistics.

3.1.2 Neural Network PDFs

A different approach is that of NN PDFs 9). They do not suffer from an a priori parametrization, nor from a tolerance criterion. Moreover, resulting PDF sets follow a Gaussian distribution, and so can be easily interpreted in a statistical way. The NN analysis that I used (1.0) is in the Zero Mass scheme for heavy quarks and bounds the strange quark distribution to be proportional to the light sea one, an assumption which is now disfavoured. The full outcome of NN analysis is a set of 1000 PDF replicas; for simulation purposes, one can use a restricted sample of 100 replicas, which already allows a meaningful error treatment.

Fig.2 shows this study for the $Z \to \mu^+\mu^-$ channel. In (a) one can see acceptance values distribution (the Gaussian fit results in $\chi^2/\mathrm{ndf} \sim 4$) and a sketch of the method used to calculate the 90% asymmetric confidence level. Fig.2(b) shows then the comparison between central values and error bands. Central values are all inside the NN error band, which seems to be a little broader than the others (both in the symmetric and in the asymmetric cases) as confirmed by the values in tab.3, which are all obtained with an an higher statistics (400000 events samples).

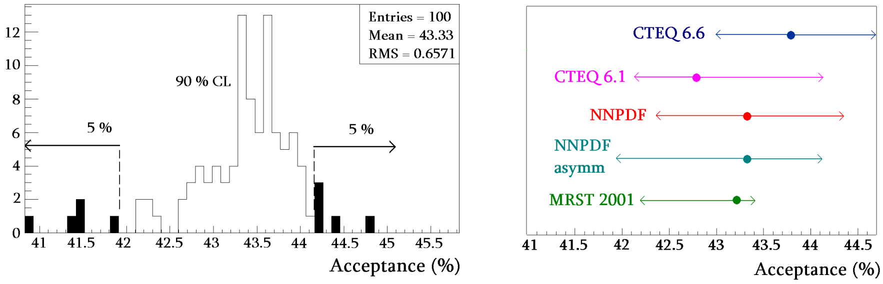

(a) (b)

Figure 2: *a) Cross sections and b) acceptances for* $pp \to W^+ \to \mu^+\nu_\mu$ *with* `Mc@Nlo` *at* $\sqrt{s} = 14$ *TeV.*

Table 3: *Comparison between acceptances calculated with different PDF sets.*

	A_0	+ ΔA	- ΔA	$\left(\max \frac{\delta A}{A}\right) \times 100$
CTEQ 6.1	42.80	1.34	0.68	3.12
CTEQ 6.6	43.75	0.93	0.77	2.12
MRST 2001	43.25	0.22	1.05	2.43
NN	43.33	1.0		2.3
Asymm NN	**43.33**	**0.83**	**1.42**	**3.3**

4 Conclusions

The results presented show that the PDFs contribution dominates geometrical acceptance uncertainty, up to $\sim 3\%$. All other effects are far less than 1%.

5 Acknowledgements

I'd like to thank G.Corcella, A.Di Ciaccio and S.Forte for useful suggestions.

References

1. The ATLAS Collaboration, JINST **3**, 2008.
2. G. Corcella *et al*, arXiv.org:hep-ph/0210213.
3. T. Sjostrand *et al*, JHEP0605 **026**, 2006.
4. S. Frixione *et al*, arXiv.org:hep-ph/0612272.
5. C. Carloni Calame *et al*, Physical Review D **69**, 2004.
6. M. Venturi, ATL-COM-PHYS-2008-251.
7. D. Stump *et al*, JHEP **0310**,2003.
8. P. Nadolsky *et al*, arXiv.org:0802.0007.
9. R. Ball *et al*, Nucl. Phys. **B809**, 2009.

Frascati Physics Series Vol. XLVIII (2009), pp. 43-48
Young Researchers Workshop: *"Physics Challenges in the LHC Era"*
Frascati, May 11 and 14, 2009

THE CMS MUON RECONSTRUCTION

Giorgia Mila
University of Turin & INFN

Abstract

One of the main goals of the Compact Muon Solenoid (CMS) design is to ensure efficient and accurate muon reconstruction.
Here a general overview of the CMS track fitting method and of the muon reconstruction process is given. Muon offline data quality monitoring and muon reconstruction certification are also discussed.

1 Introduction

The Compact Muon Solenoid (CMS) experiment 1) is one of two large general-purpose detectors for particle physics which is built at the proton-proton Large Hadron Collider (LHC) at CERN. It consists of a cylindrical barrel closed by two endcap disks and it is composed by four main detector subsystems. The innermost system is a silicon-based tracker. A scintillating crystal electromagnetic calorimeter surrounds it. A sampling calorimeter for hadrons is then placed after the electromagnetic calorimeter. The tracker and the calorimetry are compact enough to fit inside the CMS solenoid which generates a magnetic field of 3.8 T. Outside the magnet there are the large muon detectors, which are located inside the return yoke of the magnet. Since in a hadron collider leptons provide a clear signature for many of the most interesting physics processes, a precise and fast reconstruction of the leptons is mandatory for CMS. In this context the muons play a key role because their properties can be measured with great precision, as described in the following.

2 Track parameters and tracking algorithm principles

The CMS track reconstruction 2) is based on the Kalman Filter technique 3), which is a recursive method for the fit of a discrete set of data. The basic problem of this method consists in the estimation of a generic state vector $\mathbf{x}$ given a set of measurements $\mathbf{m}_k$ that are assumed to have the form

$$m_k = H_k x_{k,true} + \epsilon_k \tag{1}$$

where H_k is is the transform matrix from the state space to the measurement space and ϵ_k is the noise that affects the true state. In the case of the track reconstruction, the state vector is defined as the position and momentum relative to a given surface:

$$x = \begin{pmatrix} q/p \\ tan\phi \\ tan\theta \\ x \\ y \end{pmatrix} \tag{2}$$

where q is the charge, p is the momentum and ϕ, θ, x and y identify the track direction and position on the surface.

To complete the track description, a 5D curvilinear covariance matrix, the number of degrees of freedom and a summary of the information on the collected hits are stored in the corresponding data format.

The first step of the track reconstruction consists in the seed state estimation. For muon tracks the seed can be estimated starting from the measurements themselves or from external input. Each Kalman Filter step is then developed by two basic components:

1. *the propagator* : it extrapolate a state vector and its covariance matrix in a non-constant magnetic field, taking into account the effect of energy loss and multiple scattering in the material traversed by the track.
2. *the updator* : it includes the information from a measurement into the track.

The result of a Kalman filter is a state on the surface of the last measurement, which includes all available information. However, the trajectory parameters calculated at other points of the trajectory do not include the information from all measurements. A second iteration is used to update the parameters at every surface. In the Kalman filter terminology, this procedure is called *smoothing.* Once the hits are fitted and the fake trajectories removed, the remaining tracks are extrapolated to the point of closest approach to the beam line. In order to improve the p_T resolution a beam-spot constraint is possibly applied.

3 The muon reconstruction

Muon tracks in CMS are reconstructed at different levels and three different types of high-level muons are reconstructed. The tracks within the muon system are built combining the information coming from each muon sub-detector. This step is the so called *Stand-Alone Muon Reconstruction.* In parallel (and independently) the tracks in the tracker are reconstructed. Finally, the information from the muon spectrometer and the tracker system are combined (*Global Muon Reconstruction*) giving the final muon track. The association with the energy deposits in the calorimeters completes the muon reconstruction. Moreover a complementary approach which considers all the silicon tracker tracks and identifies them as muons by looking for compatible signatures in the calorimetric and the muon systems has been developed (*Tracker Muon Reconstruction*).

3.1 Stand-Alone muons

Their reconstruction takes into account only information from the muon spectrometer. First track segments are reconstructed locally inside each muon detector. Then the high-level reconstruction matches the information coming from different detectors to perform the tracking. A pattern of compatible segments with the muon trajectory is chosen. Then a first fit using the segment information is followed by a second more accurate fit which uses single hits

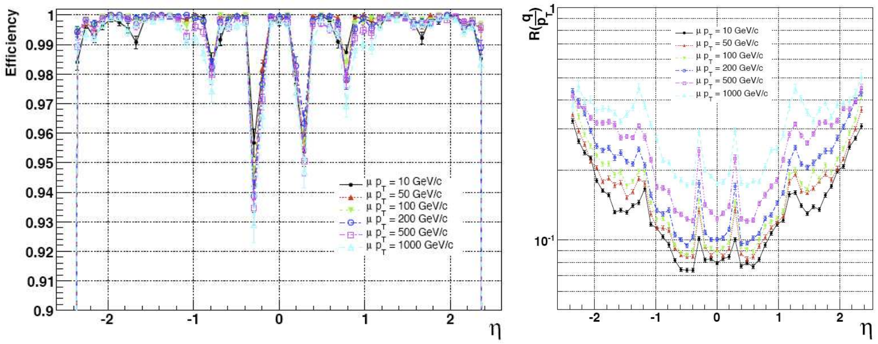

Figure 1: *p_T resolution (R) and efficiency (L) of the Stand-Alone muon reconstruction as a function of the pseudorapidity.*

which compound the segments. Fig.(1) shows its performance. The loss in efficiency at $|\eta| \sim 0.3$ is due to a geometrical effect. The $0.8 < |\eta| < 1.2$ range is the barrel-endcap overlap region. Here the seed estimation (based on a parameterization) is more difficult as segments reconstructed in different muon subdetectors are matched together. The p_T resolution is $\sim 9\%$ in the central region for muons of $p_T = 50$ GeV/c and it improves with high energies, due to the larger lever arm.

3.2 Tracker muons

Tracker muons are reconstructed starting from silicon tracker tracks identified as muon tracks. Then the algorithm searches for compatible segments in the spectrometer and minimum ionizing particle energy deposits. Fig.(2) shows the tracker tracking performance without taking into account the efficiency of the muon identification. The tracking efficiency is constant around 99.5%, except the $|\eta| \sim 0$ region where there is a dip due to the tracker geometry and the p_T resolution is $\sim 0.9\%$ in the central region for muons of p_T=50 GeV/c. As for the stand-alone tracks, the tracking resolution improves with high energies.

3.3 Global muons

The Global reconstruction combines information from different subsystems in order to obtain a more accurate description of the muon. It starts propagating

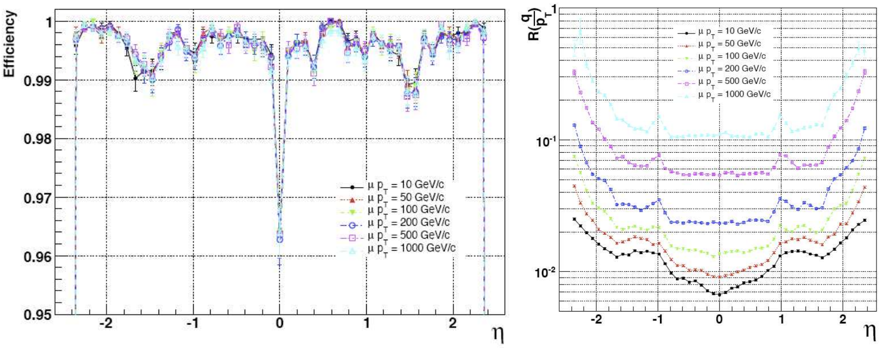

Figure 2: *p_T resolution (R) and efficiency (L) of the silicon tracker reconstruction as a function of the pseudorapidity.*

the stand-alone muon tracks inside the tracker. Therefore a spatial region is chosen and the best tracker track which matches with the muon stand-alone track is selected. Finally a global refit using the hits from the tracker and the stand-alone tracks is done. In this way the muon reconstruction can exploits the long lever arm of CMS. The Global muon efficiency and resolution behaviour depends respectively on the Stand-Alone and the Tracker reconstruction, as shown in Fig.(3).

4 Offline Monitoring of the muon reconstruction

The main task of the offline monitoring of the muon reconstruction is the data certification for physics analysis. The offline monitoring runs on the full statistics during the prompt reconstruction which has one day of delay with respect to the online data taking. A list of histograms crucial to understand the muon collection properties is produced and quality tests are applied to them in order to provide a list of flags which indicate the goodness of all the muon reconstruction components. Finally, the results are published on a web page.
The muon collection is a complex object to be certificated because the muon reconstruction does not only depend on tracking algorithm but it involves many other information, such as the calorimetric deposits and the muon identification variables. Therefore the combination of the results from the quality tests is important to univocally certificate the muon reconstruction for a given data

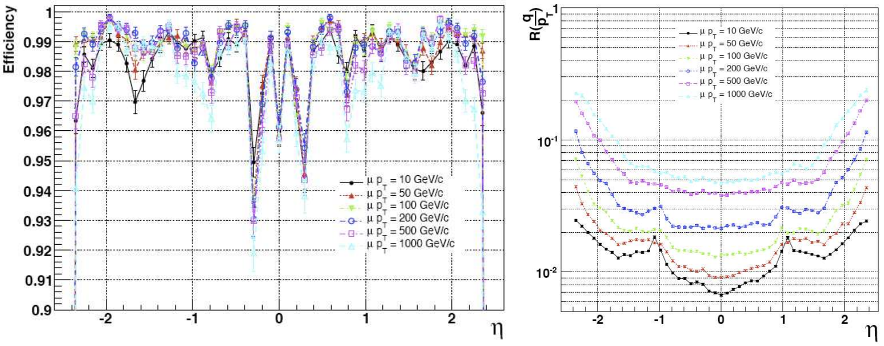

Figure 3: *p_T resolution (R) and efficiency (L) of the Global muon reconstruction as a function of the pseudorapidity.*

sample. The main variables monitored are:

- Track parameters and quality variables (*e.g.* χ^2, number of hits).
- Muon energy deposits, separately for each type of calorimeter.
- Muon identification quantities, *e.g.* residuals between segments in the muon chambers and extrapolated track states.

The ranges of the quality tests have been tuned on simulated events for both cosmics and proton-proton collision data. Summary histograms of the test results are provided for shifters and the complete certification procedure has been checked, used and improved during the detector commissioning with cosmics.

References

1. R. Adolphi et al. [CMS Collaboration] , *The CMS experiment at the CERN LHC*, JINST **3** (2008) S08004.
2. R. Bellan, *Study and Development of the CMS High Level Trigger and Muon Reconstruction Algorithms*, CMS TS-2008/021.
3. R. Fruhwirth, *Application of Kalman filtering to track and vertex fitting*, Nucl. Instrum. Meth. **A262** (1987) 444.

Frascati Physics Series Vol. XLVIII (2009), pp. 49-54
Young Researchers Workshop: *"Physics Challenges in the LHC Era"*
Frascati, May 11 and 14, 2009

HEAVY VECTOR PAIR PRODUCTION AT LHC IN THE CHIRAL LAGRANGIAN FORMULATION

Antonio Enrique Cárcamo Hernández
Scuola Normale Superiore Di Pisa, Pisa, Italy

Abstract

The total cross sections for Heavy vector pair production at LHC by longitudinal gauge boson fusion and Drell Yan annihilation are studied as a function of the mass M_V of the vector in the framework of the Chiral Lagrangian formulation with massive spin one fields. The cross section for V^+V^- production in e^+e^- collisions at $\sqrt{s} = 3TeV$ is also studied.

1 Introduction

In spite of the very good agreement of the Standard Model predictions with experimental data, the Higgs boson has not been detected experimentaly and then the mechanism of electroweak symmetry breaking responsible for the generation of the masses of the fermions and bosons remains to be explained. Besides that, the Standard Model does not explain the scale of the electroweak

symmetry breaking, which is a free parameter of the theory, taken from the experiment. Moreover, the Standard model has the so called hierarchy problem, which is the instability of the Higgs field against quantum corrections.
Since there is no experimental evidence for a Higgs particle up to date, it is natural to ask what happens if we keep all the standard model fields, except the Higgs boson. With this motivation and inspired in the Chiral Perturbation Theory Lagrangian formalism up to $O\left(p^4\right)$ developed by Ecker et al., Barbieri et al have introduced a $SU\left(2\right)_L \times SU\left(2\right)_R$ Chiral Lagrangian with two massive spin one tensor fields of opposite parity which interact with the Goldstone bosons and with the Standard Model gauge fields. This Chiral Lagrangian formulation with massive spin one tensor fields of opposite parity, which is meant to be valid up to a cutoff $\Lambda \simeq 4\pi v \simeq 3TeV$ can account for the Electroweak Precision Tests and keep the unitarity of the longitudinal W boson scattering under control up to $3TeV$ 1). Since in the mentioned Chiral Lagrangian formulation with massive spin one tensor fields, unitarity of longitudinal W boson scattering is preserved up to $3TeV$, these spin one tensor fields play the role of the Higgs boson in keeping unitarity under control.

2 Effective Chiral Lagrangian with massive spin 1 fields.

Chiral Lagrangians have been extensively used to describe the phenomenon of spontaneuos symmetry breaking in strong and in weak interactions. They can be regarded as the low energy limit of an underlying fundamental theory 2, 3, 4). Inspired in the Chiral Perturbation Theory Lagrangian formalism up to $O\left(p^4\right)$ developed by Ecker et al. used in the description of the low energy effects in QCD, the following $SU\left(2\right)_L \times SU\left(2\right)_R$ invariant Lagrangian at $O\left(p^2\right)$ describing the coupling of heavy fields $V^{\mu\nu}$ and $A^{\mu\nu}$ to Goldstone bosons and Standard Model gauge fields, invariant under parity is considered 1):

$$\begin{aligned}
\mathcal{L}_{eff} &= \frac{v^2}{4} Tr\left(D_\mu U \left(D^\mu U\right)^\dagger\right) - \frac{1}{2}\sum_{R=V,A} Tr\left(\nabla^\lambda R_{\lambda\mu}\nabla_\nu R^{\nu\mu} - \frac{1}{2}M_V^2 R_{\mu\nu}R^{\mu\nu}\right) \\
&\quad + \frac{i}{2\sqrt{2}} G_V Tr\left(V^{\mu\nu}\left[u_\mu, u_\nu\right]\right) + \frac{F_V}{2\sqrt{2}} Tr\left[V^{\mu\nu}\left(uW_{\mu\nu}u^\dagger + u^\dagger B_{\mu\nu}u\right)\right] \\
&\quad + \frac{F_A}{2\sqrt{2}} Tr\left[A^{\mu\nu}\left(uW_{\mu\nu}u^\dagger - u^\dagger B_{\mu\nu}u\right)\right] \qquad (1)
\end{aligned}$$

where the covariant derivate ∇_μ acting on the $V_{\mu\nu}$ and $A_{\mu\nu}$ antisymmetric spin one tensor fields is defined as:

$$\nabla_\mu R = \partial_\mu R + [\Gamma_\mu, R]\,, \qquad R_{\mu\nu} = \frac{1}{\sqrt{2}}\tau^a R^a_{\mu\nu}, \qquad R = V, A$$

$$\Gamma_\mu = \frac{1}{2}\left[u^\dagger\left(\partial_\mu - i\widehat{B}_\mu\right)u + u\left(\partial_\mu - i\widehat{W}_\mu\right)u^\dagger\right], \qquad u = e^{i\frac{\pi}{2v}}, \qquad \pi = \pi^a\tau^a$$

$$u_\mu = u_\mu^\dagger = iu^\dagger D_\mu U u^\dagger = iu^\dagger\left(\partial_\mu U - i\widehat{B}_\mu U + iU\widehat{W}_\mu\right)u^\dagger, \qquad U = u^2$$

being $\widehat{W}_\mu = \frac{g}{2}\tau^a W^a_\mu$, $\widehat{B}_\mu = \frac{g'}{2}\tau^3 B_\mu$ and Γ_μ the connection which contains Goldstone bosons and the Standard Model Gauge fields and U an exponential representation of $SU(2)$ which incorporates the pions field. In the previous chiral effective Lagrangian, the Goldstone bosons are incorporated into non linear representations $SU_L(2) \times U(1)_Y$ symmetry group such that the mentioned Lagrangian has an $SU_L(2) \times U(1)_Y$ invariance. In the unitary gauge $U = 1$, the Lagrangian for the Goldstone bosons reduces to the mass terms for the gauge bosons. In the limit where the coupling g' is neglected, the Lagrangian given in (1) has the custodial symmetry and the mass of the W and Z bosons are equal, which implies that the ρ parameter at tree level is equal to one. The pions transforms like a triplet under the custodial symmetry group $SU(2)_{L+R}$, which plays the role of the isospin group when low energy pions interactions are considered.

3 Heavy vector pair production at LHC by gauge boson fusion.

The Figures 1a (left) and 1b (right) show the total cross sections at LHC computed by using VBA (Vector Boson Approximation) for all the processes of longitudinal vector production and vector production by longitudinal gauge boson fusion at $\sqrt{s} = 14TeV$ and $G_V = 200GeV$. The leading-order parton distribution functions CTEQ5M for quarks have been used. One has that the transverse and the interference between the transverse and longitudinal polarizations states of the vectors V' leads to total cross sections for the processes $pp \to G_L G'_L qq \to VV'qq$ with $G, G' = W, Z$ much bigger than the corresponding to the processes $pp \to G_L G'_L qq \to V_L V'_L qq$, respectively. It can be seen that the most important longitudinal vector and vector production processes are $pp \to W_L^+ W_L^+ qq \to V_L^+ V_L^+ qq$ and $pp \to W_L^+ Z_L qq \to V^+ V^0 qq$, respectively.

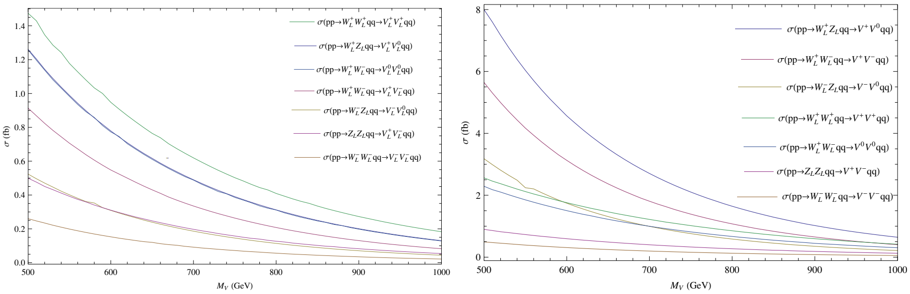

Figure 1: *a) Total cross sections at LHC for the processes of longitudinal vector production by longitudinal vector boson fusion b) Total cross sections at LHC for the processes of vector production by longitudinal vector boson fusion.*

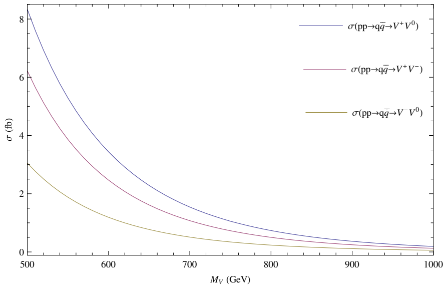

Figure 2: *Total cross sections at LHC for $V^{\pm}V^0$ and V^+V^- vector production processes by Drell Yan annihilation.*

We have checked that the contribution of intermediate transverse gauge bosons is negligible.

4 Total cross section at LHC for the $V^{\pm}V^0$ and V^+V^- production through Drell Yan annihilation.

The Figure 2 shows the total cross sections at LHC for the $V^{\pm}V^0$ and V^+V^- production through Drell Yan annihilation in proton proton collisions through the processes $pp \to q\overline{q} \to V^{\pm}V^0$ and $pp \to q\overline{q} \to V^+V^-$ in terms of the mass M_V of the vector for $\sqrt{s} = 14TeV$ (LHC center of mass energy). The leading-order parton distribution functions CTEQ5M for quarks have been used. It can be seen that the most important VV production process in proton-proton collisions is through the Drell Yan annihilation with pairs of positive charged V^+ and neutral V^0 in the final state. For the lightest vector of mass $M_V = 500GeV$, the total cross section at LHC for the V^+ and V^0 production through Drell Yan mechanism is $8.34fb$ and for the very heavy vector of mass $M_V = 1TeV$, this total cross section is strongly supressed and has the value of $0.19fb$. The second most relevant production process of pairs of V's through Drell Yan mechanism is in a pair of positive charged V^+ and a negative charged V^-, whose total cross section at LHC takes the values of $6.22fb$ and $0.13fb$ for $M_V = 500GeV$ and $M_V = 1TeV$, respectively. We notice that the total cross sections at LHC for vector production by gauge boson fusion and Drell Yan annihilation are numerically comparable. This results from a combination of the different partonic luminosities ($q\bar{q}$ versus GG) and of the different high energy behaviour of the partonic cross sections, of which only $GG \to VV$ grows with the center of mass energy.

5 Cross section for the V^+V^- production in e^+e^- collisions.

The Figure 3 shows the cross section for the V^+V^- production in e^+e^- collisions at $\sqrt{s} = 3TeV$. It can be seen that the most important V^+V^- production process is through e^+e^- collisions, since the cross section has the value of $107.24fb$ for the lightest vector of mass $M_V = 500GeV$. For a very heavy vector of mass $M_V = 1TeV$, the cross section for the V^+V^- production in e^+e^- collisions takes the value of $18.61fb$.

6 Conclusions

If heavy vectors exist with a mass in the $500 - 1000$ GeV range, they will most likely be discovered at LHC in single production or in association with one standard gauge boson 1). To understand the underlying physics, this will most likely not be enough. For this reason we have studied the pair production at LHC, which is in the few fb range, depending on the specific process. The transverse polarization states and the interference between longitudinal and transverse polarization states of V give a significant contribution to the total cross sections for vector production processes. It is found that total cross

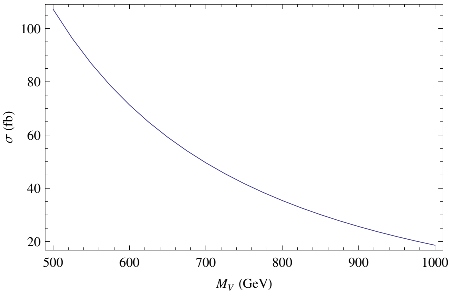

Figure 3: *Total cross sections for the* V^+V^- *production in* e^+e^- *collisions*

sections at LHC for vector production and Drell Yan annihilation have similar values and that the most relevant vector production processes corresponds to a pair of positive charged and neutral vectors in the final state. It is also important to mention that charged vector production process in e^+e^- collisions is very promising. Further detailed studies will have to be made to assess the detectability of these processes above the Standard Model backgrounds.

7 Acknowledgements

The author thanks Professor Riccardo Barbieri for introducing him to this field, for carefully reading of the article and for very useful discussions. Author also thanks R. Torres, G. Corcella and R. Trincherini for very useful discussions.

References

1. R. Barbieri, G. Isidori, V. S. Rychkov and E. Trincherini, Phys. Rev. **D 78**, 036012 (2008) [arXiv:hep-ph/0806.1624v1].
2. G. Ecker et al, Phys. Rev. Lett. **B 223** (1989) 425; Nucl. Phys. **B 321** (1989) 311
3. A. V. Manohar, arXiv:hep-ph/9606222v1.
4. A. Pich, arXiv:hep-ph/9806303v1.

Frascati Physics Series Vol. XLVIII (2009), pp. 55-60
YOUNG RESEARCHERS WORKSHOP: *"Physics Challenges in the LHC Era"*
Frascati, May 11 and 14, 2009

MASS DEGENERATE HEAVY VECTOR MESONS AT HADRON COLLIDERS

Mark Round
Swansea University, School of Physical Sciences,
Singleton Park, Swansea, Wales, UK

Abstract

We study the LHC phenomenology of two mass-degenerate heavy gauge bosons with the quantum numbers of the Z and γ. We give a leading-order estimate of the number of events expected in Drell-Yan processes in terms of the model and machine parameters. We consider the feasibility of measuring a forward-backward asymmetry for various choices of the parameters and estimate the reach. We comment on how the results may affect future collider design.

1 Introduction

The main purpose of the LHC is to discover the origin of electro-weak (EW) symmetry breaking and what new physics lies at the TeV scale.

One clean signal for the LHC would be the discovery of new, higher-mass copies of the standard-model (SM) gauge fields. For such a scenario, the LHC reach in observable masses and couplings is of interest. Motivations for this study include weakly coupled SM extensions with new heavy vector fields (1), little Higgs models (2) and technicolor (TC) (3).

In this paper, we consider the scenario in which a complete set of four spin-1 copies of the SM gauge bosons with heavy degenerate masses are produced in *pp* collisions and detected via the decay into muons. The muon channel is expected to have a low background at the LHC. For simplicity, we model the decay width of these particles by assuming it to be dominated by the decay into SM fermions, hence avoiding complications (and model-dependencies) arising when including the decay into light scalars and gauge bosons.

In the SM, a forward-backward asymmetry arises from interference terms between virtual processes with the exchange of Z and γ, and it is a very sizable effect even in the TeV energy range. Measuring such an effect at a hadron collider is onerous but a method and its use at the LHC was surveyed by Dittmar (4). Measuring an asymmetry at a new neutral pole would indicate it is made of two different exchange particles.

2 Model Phenomenology

We model the new neutral resonances by adding an extra set of $SU(2) \times U(1)$ gauge fields into the SM electro-weak Lagrangian. We assume that some mechanism spontaneously breaks the $SU(2)^2 \times U(1)^2$ gauge symmetry to the SM $SU(2)_L \times U(1)_Y$ above the TeV scale, and that in the process a copy of the W, Z and γ all aquire a similar mass m. We also assume that the couplings of the heavy gauge bosons to the SM currents can be written as Rg_{SM}, where g_{SM} stands for the coupling of the W, Z and γ. The common mass, m, and the coupling ratio R are the only parameters.

In this scenario one can compute the Drell-Yan event rate, N, with a PDF package and indeed, it can be approximated by (5),

$$N \propto \frac{sLR}{m^4}, \tag{1}$$

up to a proportionality constant that contains the electro-weak couplings and the normalization of the PDF distribution. For this study we used the Fermi02 set (6) & (7).

Discovery of the new resonance depends on some value of the ratio N/L of the event number N and the machine luminosity L. The approximate event rate can be solved for R given m at various machine energies and luminosities producing Figs. 1(a) and 1(b). These two plots show how improving the energy of a hadron collider compared to increasing the luminosity affects the search.

Take the $N/L = 3$ fb curve. If one were to triple the luminosity of the machine that would imply moving to the next curve on the right. However if one were to improve the machine energy from 10 TeV to 24 TeV that would mean moving from Fig. 1(a) to Fig. 1(b). By improving the luminosity by a factor of 20, one may move from a reach in masses below 2.2 TeV to roughly 3.3 TeV at a 10 TeV machine. Whilst improving the collision energy takes the reach to well above 4.0 TeV, even at low luminosity.

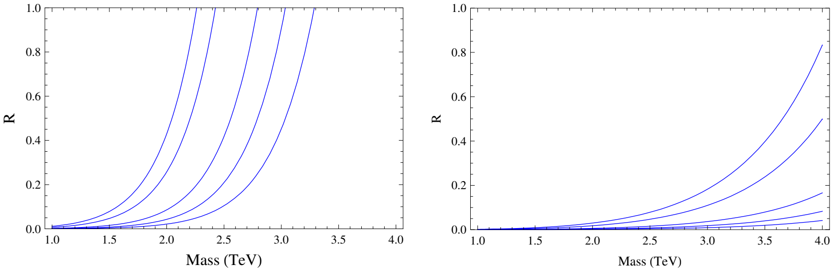

(a) $\sqrt{s} = 10\ TeV$ (b) $\sqrt{s} = 24\ TeV$

Figure 1: *The minimal coupling R for various choices of the event number N divided by the luminosity L for two machine energies. From the left, $N/L =$* $5, 3, 1, 1/2, 1/4$ fb.

2.1 Forward-Backward Asymmetry

Consider the angular distribution of $3/8(1+\cos^2\theta)+A_{FB}\cos\theta$ as a probability distribution function. This distribution has a mean defined as

$$\langle\hat{\theta}\rangle = \int \hat{\theta} g(\hat{\theta}) \sin\hat{\theta} d\hat{\theta} = \frac{\pi}{4}(2 - A_{FB})\,, \tag{2}$$

while

$$\sigma_p^2 \equiv \int \left(\hat{\theta}^2 - \langle\hat{\theta}\rangle^2\right) g(\hat{\theta}) \sin\hat{\theta} d\hat{\theta}\,. \tag{3}$$

Interestingly, A_{FB} turns out to be just proportional to $\langle\hat{\theta}\rangle$. Hence we can estimate the statistical error on the extraction of the symmetry as

$$\Delta A_{FB}^{\mathrm{stat}} = \frac{4\sigma_p}{\pi\sqrt{n-1}}\,, \tag{4}$$

where n is the number of events used to study the angular distribution.

Secondly there is an error introduced by the methodology (see $^{4)}$). The assumption that the initial quark direction be always the one of the outcoming γ' or Z', implies a possible misidentification $\hat{\theta} \leftrightarrow \pi - \hat{\theta}$. Let the probability of mis-identification be p, then in a sample of n events np are mis-identified. Let n_F (n_B) events travel in the forward (backward) direction. Then $n = n_F + n_B$. The worst case scenario would be that all np events were placed in n_F but should have been placed in n_B. In this case the difference in true and measured asymmetry would be,

$$\Delta A_{FB}^{\mathrm{sys}} \quad = \quad \pm 2p \tag{5}$$

This means that adding the method and statistical errors together the total error wil be,

$$\Delta A_{FB} = \frac{4\sigma_p}{\pi\sqrt{n-1}} + 2p(Y_c), \tag{6}$$

where the dependence of p on the cut Y_c has been added for clarity. We conservatively add the two sources of error linearly.

Now we can define $P(Y_c)$, the fraction of events with $|Y| > Y_c$. Then, the number of events used to extract the asymmetry is,

$$n = PN. \tag{7}$$

Requiring that $\Delta A_{FB} < \mathscr{E}$ (for $\mathscr{E} > 2p$) implies

$$n > \left(\frac{4\sigma_{pop}}{\pi(\mathscr{E} - 2p}\right)^2 + 1 \tag{8}$$

or equivalently,

$$N > \frac{1}{P}\left[\left(\frac{4\sigma_{pop}}{\pi(\mathscr{E} - 2p}\right)^2 + 1\right] \tag{9}$$

total events.

For the model considered, the asymmetry is $A_{FB} \simeq -0.42$ $^{5)}$. The asymmetry with the SM particles and one new resnonance is very small. Therefore seeing an asymmetry at a collider would indicate that there are two particles in the new neutral resonance.

To measure such an effect at a collider one would require an error $\mathscr{E} < 0.14$ in order to conclude, at the 3σ level, an asymmetry is present. Consider the case that all events happen to fall precisely at the rapidity cut Y_c. Then the probability p is calculable, yielding a conservative estimate: with real data having $|Y| > Y_c$ in general the error probability will be smaller than this p. The fraction P can also be computed.

From this we can then find the minimum number of events for a given asymmetry at various masses. Then using the formula to convert between events and parameter space derived earlier we can plot the results. The results of this process are shown in Figs. 2(a) and 2(b).

Figure 2(a) shows that large increases in luminosity lead to modest gains in reach, compared to the gain obtained by going to larger energies, as shown in Fig. 2(b).

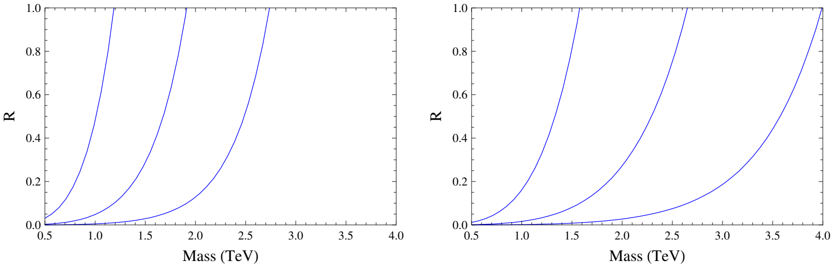

(a) $\sqrt{s}$ =*14 TeV*

(b) $\sqrt{s}$ =*24 TeV*

Figure 2: *Minimal coupling* R*, as a function of the mass* m*, required to observe a* 3σ $A_{FB} \sim -0.42$ *at the resonance for* $L = 1, 10, 100$ fb^{-1} *at two different energies of hadron collider*

3 Conclusions

We performed a model-independent study of the Drell-Yan processes at the LHC, assuming that two new gauge bosons with quantum numbers and couplings analogous to the photon and Z boson, but rescaled by a common factor of $R < 1$, have masses so close to each other that their kinematic peaks are indistinguishable.

For a 10 TeV collider, and luminosities in the $2 - 40\text{fb}^{-1}$, bounds on new resonances no higher than 3 TeV can be obtained. With a 24 TeV collider the region well over 4 TeV can be explored, depending on the specific coupling R.

As for the forward-backward asymmetry, we provided a simple estimate formula that ignored experimental issues. The collider ability to measure an asymmetry at the 3σ level is heavily restricted to light masses. Even at very high luminosities measuring the asymmetry for masses of 3 TeV is out of reach for a 14 TeV collider, even in principle. By contrast, at a 24 TeV machine the reach is far larger. This is as a result of the PDF scaling offering a larger fraction of high rapidity events with higher energy. At such a machine it may be possible to measure asymmetries and greatly restrict currently open parameter spaces.

4 Acknowledgements

The author wishes to thank M. Piai for useful comments on the manuscript.

References

1. See for instance T. Appelquist, B. A. Dobrescu and A. R. Hopper, Phys. Rev. D **68**, 035012 (2003) [arXiv:hep-ph/0212073], and references therein.

2. See for instance N. Arkani-Hamed, A. G. Cohen, E. Katz and A. E. Nelson, JHEP **0207**, 034 (2002) [arXiv:hep-ph/0206021]; I. Low, W. Skiba and D. Tucker-Smith, Phys. Rev. D **66**, 072001 (2002) [arXiv:hep-ph/0207243].

3. S. Weinberg, Phys. Rev. D **19**, 1277 (1979); L. Susskind, Phys. Rev. D **20**, 2619 (1979); S. Weinberg, Phys. Rev. D **13**, 974 (1976).

4. M. Dittmar, Phys. Rev. D **55**, 161 (1997) [arXiv:hep-ex/9606002].

5. M. Piai and M. Round, arXiv:0904.1524 [hep-ph].

6. M. R. Whalley, D. Bourilkov and R. C. Group, arXiv:hep-ph/0508110.

7. W. T. Giele, S. A. Keller and D. A. Kosower, arXiv:hep-ph/0104052.

Frascati Physics Series Vol. XLVIII (2009), pp. 61-66
Young Researchers Workshop: *"Physics Challenges in the LHC Era"*
Frascati, May 11 and 14, 2009

STUDY OF $B \to K\eta_c$ AND $B \to K\eta_c(2S)$ DECAYS

Anna Vinokurova (for the Belle collaboration)
Budker Institute of Nuclear Physics

Abstract

A data sample of 535 million $B\bar{B}$ meson pairs collected in the Belle experiment at the KEKB e+e- collider has been used to study properties of the η_c and its excited state $\eta_c(2S)$ mesons produced in B decay to K and charmonium. We use the decay of charmonium to $K_S K \pi$ to study the effects of interference between signal events and events of the B decay into the same final state without intermediate charmonium. Taking this interference into account we obtain masses, widths, and decay branching fractions of the η_c and $\eta_c(2S)$ mesons. The results agree with the world average values and for the first time the intereference effects are taken into account.

1 Introduction

The decay $B^\pm \to K^\pm c\bar{c}$ is a copious source of charmonia. The η_c branching fractions were measured with poor accuracy and can be improved. The $\eta_c(2S)$

meson was seen in one hadronic decay only ($\eta_c(2S) \to K_S K^\pm \pi^\mp$) and requires some additional study. It can be easily done using the analysis algorithm similar to the one for η_c. The following decays of B mesons were studied:

$$B^\pm \to K^\pm \eta_c \to K^\pm K_S K^\pm \pi^\mp, \tag{1}$$

$$B^\pm \to K^\pm \eta_c(2S) \to K^\pm K_S K^\pm \pi^\mp. \tag{2}$$

The analysis was performed using the Belle detector 1). Considered statistics is rather high – 492 fb^{-1} and gives an opportunity to determine masses and widths of η_c and $\eta_c(2S)$ mesons.

2 Event selection

A data sample of 492 fb^{-1} (535 million $B\bar{B}$ events) collected at the $\Upsilon(4S)$ resonance is used in this analysis. In this analysis K candidates decay via the $\pi^+\pi^-$ mode.

Charged tracks are selected with requirements based on the average hit residuals and impact parameters relative to the interaction point. We require that the polar angle of each track be in the angular range of $18^\circ - 152^\circ$ and that the track transverse momentum be greater than 100 MeV/c.

Charged kaon candidates are identified by the requirement $\mathcal{R}(K) > 0.6$, which has an efficiency of 90% and a pion misidentification probability of approximately $(3 - 10)\%$. For pion candidates we require $\mathcal{R}(\pi) > 0.2$.

B meson candidates are identified by their center-of-mass (c.m.) energy difference $\Delta E = (\sum_i E_i) - E_\mathrm{b}$, and the beam-constrained mass $M_\mathrm{bc} = \sqrt{E_\mathrm{b}^2 - (\sum_i \vec{p}_i)^2}$, where $E_\mathrm{b} = \sqrt{s}/2$ is the beam energy in the $\Upsilon(4S)$ c.m. frame, and $\vec{p}_i$ and E_i are the c.m. three-momenta and energies, respectively of the B meson candidate decay products.

To suppress the large continuum background ($e^+e^- \to q\bar{q}$, where $q = u, d, s, c$), topological variables are used. Since the produced B mesons are almost at rest in the c.m. frame, the signal event shapes tend to be isotropic while continuum $q\bar{q}$ events tend to have a two-jet structure. We use the angle between the thrust axis of the B candidate and that of the rest of the event (Θ_thrust) to discriminate between these two cases. The distribution of $|\cos\Theta_\mathrm{thrust}|$ is strongly peaked near $|\cos\Theta_\mathrm{thrust}| = 1$ for $q\bar{q}$ events and is nearly flat for $\Upsilon(4S) \to B\bar{B}$ events. We require $|\cos\Theta_\mathrm{thrust}| < 0.8$.

Data sample can contain events of decays which have the same final state as the studied one but their intermediate states differ from the required ones. We call these events non-resonant component. This component can interfere with the signal. To discover unwanted intermediate states we check the consistency of invariant mass combinations with different meson mass values. If some combination forms such narrow resonances as D, D_S, and φ mesons, the interference is negligible and such event can be excluded from the analysis.

From data sample corresponding to one event one can find several combinations, which satisfy the selection criteria. Since each event contains not more than one real B meson, which decays in the required way, getting several candidates in one event points to the fact that one of them is reconstructed incorrectly. In that case the B candidate is chosen taking into account values of such parameters as invariant masses of reconstructed particles, vertex coordinate, etc.

3 Interference study

In the decay $B \to K^{\pm}K_SK\pi$ there are 4 particles in the final state which gives 4×3 measured parameters. Taking into account 4 constraints of energy-momentum conservation and integrating over 3 angles of B decay (it is a pseudoscalar and there should be no dependence on these angles) we have 5 independent variables to describe the process amplitude. We chose the following parameters: $K_SK\pi$ invariant mass, two Dalitz variables of $\eta_c(\eta_c(2S))$ decay q_1^2 and q_2^2 (for example, $M^2_{K\pi}$ and $M^2_{K_S\pi}$), angle between K_S and K from B decay in the rest frame of $KK_S\pi$ system (θ), and angle between the planes of $K-\pi$ and $K-K_S$ in the same system (ϕ). Due to low statistics we don't use angle ϕ or Dalitz plot to extract non-resonant contribution. For our study we use $M(K_SK\pi)$ and $cos\theta$ distributions. In the signal region invariant mass distribution has four peaks at the masses of charmonium states η_c, J/ψ, χ_{c1}, and $\eta_c(2S)$ (in order of mass increase) – see Fig. 1. In case of non-resonant component this distribution is described by a smooth function. Another variable which can be used for the amplitudes separation is $\cos\theta$. Since η_c and $\eta_c(2S)$ are pseudoscalars ($J^P = 0^-$) we expect uniform distribution over $\cos\theta$. In Fig. 2(a,b) the distribution for θ angle are presented for $M(\eta_c)$ signal and sideband regions. One can see that the sideband distribution has contributions of higher (P and D) angular waves.

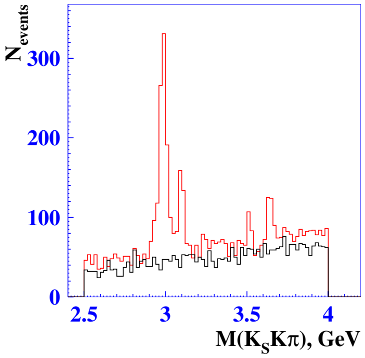

Figure 1: *Red histogram shows signal distribution of invariant mass* ($K_SK^{\pm}\pi^{\mp}$) *in the decay* $B^{\pm} \rightarrow K^{\pm}K_SK^{\pm}\pi^{\mp}$. *Black histogram demonstrates combinatorial background*

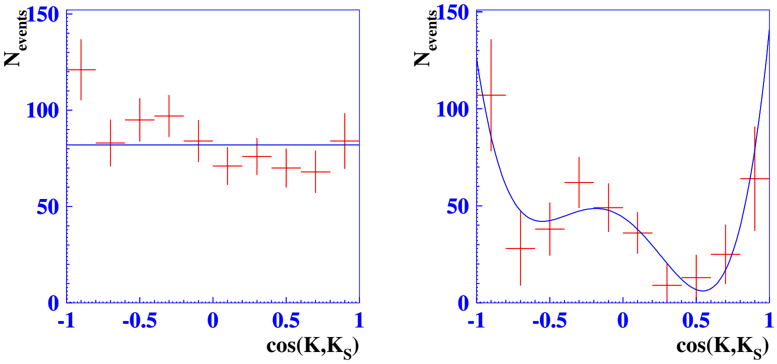

Figure 2: *Distribution over angle* θ *(a) for the* η_c *signal region; (b) for the* η_c *sideband region*

Thus we perform a 2-D fit of $m_{KK_S\pi}$–$\cos\theta$ assuming that the non-resonant signal amplitude is constant within the mass ranges (2.5 – 3.46) and (3.14 – 4.06) GeV[1]. The fitting function can be presented as a squared module of the

---

[1] We exclude J/ψ region (3.07 – 3.13 GeV) from the fit because the inter-

sum of the signal and non-resonant amplitudes integrated over all variables except $M_{K_S K\pi}$ and $\cos\theta$:

$$\begin{aligned} F(s,x) \quad = \quad & \int\int\int\int_{x-\frac{\delta}{2}}^{x+\frac{\delta}{2}}\int_{s-\frac{\Delta}{2}}^{s+\frac{\Delta}{2}}(1+\varepsilon_1 x'+\varepsilon_2 x'^2) \\ & \left|\left(\frac{\sqrt{N}}{s'-M^2+iM\Gamma}A_\eta(q_1^2,q_2^2)+\alpha A_S(q_1^2,q_2^2)\right)S(x')+\right. \\ & \left.\beta A_P(q_1^2,q_2^2)P(x')+\gamma A_D(q_1^2,q_2^2)D(x')\right|^2 ds'dx'dq_1^2dq_2^2d\phi, \quad (3) \end{aligned}$$

- $x = cos(\theta)$, $s = M(K_S K\pi)^2$;
- ε_1 and ε_2 – constants which characterise efficiency dependence on x and are determined from MC;
- A_η – signal S-wave amplitude, $A_{S,P,D}$ - background S-, P-, and D-wave amplitudes respectively[2].

Fit projections are shown in Fig. 3.

4 Results and discussion

All the studied sources of systematics uncertainties for branching products and charmonium masses and widths are listed in 2). In most of the cases the error coming from the bin size variation is dominant.

Model error comes from the uncertainty of the interference between signal and non-resonant contribution.

As a result for the η_c decay we get the number of signal events $N = 840 \pm 50(stat) \pm 180(model)$. One can compare it to the result in the assumption of no interference 2): $N = 790 \pm 40(stat)$.
For the branching product we get $\mathcal{B}(B^\pm \to K^\pm \eta_c) \times \mathcal{B}(\eta_c \to K_S K^\pm \pi^\mp) = (20.5 \pm 1.2(stat)^{+1.4}_{-2.2}(syst) \pm 4.4(model)) \times 10^{-6}$.

---

ference term of J/ψ and non-resonant signals is negligible due to the small width of the former and it does not help in determination of the interference contribution with η_c. The same arguments refer to the exclusion of χ_{c1} region (3.48 – 3.54 GeV).

[2] Other variables are described in 2).

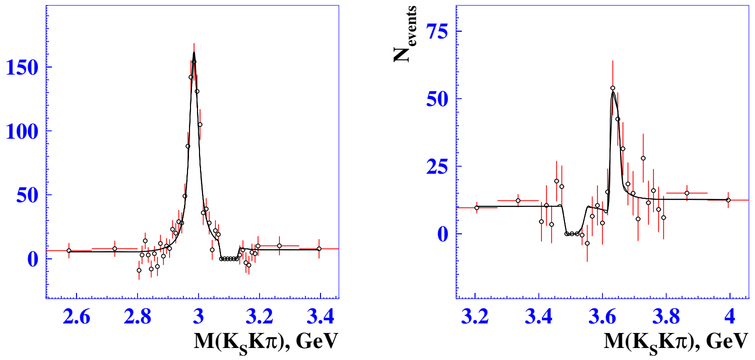

Figure 3: *Projections of the fits of the distributions over $K_SK\pi$ invariant mass in η_c and $\eta_c(2S)$ mass regions*

Parameters of the η_c meson:
$M = (2984.2 \pm 1.2(stat)^{+0}_{-1.8}(syst) \pm 0.2(model))$ MeV;
$\Gamma = (30.7 \pm 2.3(stat)^{+0.4}_{-1.2}(syst) \pm 0.4(model))$ MeV.

Similarly, for the $\eta_c(2S)$ decay we obtain $N = 102 \pm 26(stat) \pm 38(model)$. In the assumption of no interference the number of events is $N = 130 \pm 30(stat)$. The branching product is $\mathcal{B}(B^{\pm} \to K^{\pm}\eta_c(2S)) \times \mathcal{B}(\eta_c(2S) \to K_SK^{\pm}\pi^{\mp}) = (2.2 \pm 0.6(stat)^{+0.6}_{-0.1}(syst) \pm 0.8(model)) \times 10^{-6}$.
Parameters of the $\eta_c(2S)$ meson:
$M = (3638.2 \pm 2.3(stat)^{+1.3}_{-2.4}(syst) \pm 0.8(model))$ MeV;
$\Gamma = (6.0^{+13.3}_{-1.4}(stat)^{+8.1}_{-0.8}(syst) \pm 2.5(model))$ MeV.

5 Acknowledgments

I thank the KEKB group for the excellent operation of the accelerator and my colleagues from the Belle collaboration for numerous useful discussions.

References

1. A. Abashian *et al.* (Belle Collaboration), Nucl. Instr. and Meth. A **479**, 117 (2002).

2. To be published.

Frascati Physics Series Vol. XLVIII (2009), pp. 67-72
YOUNG RESEARCHERS WORKSHOP: *"Physics Challenges in the LHC Era"*
Frascati, May 11 and 14, 2009

CONTINUUM SUPPRESSION IN THE RECONSTRUCTION OF $B^0 \to \pi^0\pi^0$

T. Danger Julius
The University of Melbourne Parkville, Victoria Australia 3010

Abstract

This proceeding explores the improvement of the measurement of the branching fraction of $B \to \pi^0\pi^0$, and how it is possible to tighten the bound on the angle ϕ_2, a parameter that describes CP violation within the Standard Model.

1 CP Violation

The weak eigenstate of a quark is not its mass eigenstate, but the relationship between the two can be expressed using the 3x3 Cabibbo-Kobayashi-Maskawa (CKM) matrix. This matrix is unitary and contains a complex phase that can accomodate CP violation within the Standard Model (SM).

$$\begin{pmatrix} d \\ s \\ b \end{pmatrix} = \begin{pmatrix} V_{ud} & V_{us} & V_{ub} \\ V_{cd} & V_{cs} & V_{cb} \\ V_{td} & V_{ts} & V_{tb} \end{pmatrix} \begin{pmatrix} d' \\ s' \\ b' \end{pmatrix} \tag{1}$$

Equation 1 shows the CKM matrix with primed values representing the mass eigenstates, and unprimed representing the weak eigenstates. The relationship between entries the elements of the matrix can be represented graphically as a triangle on the complex plane, with angles representing the relative phases between matrix elements. By finding the magnitudes of the sides and the angles of this triangle, we can test the predictions of the SM, and perhaps uncover new physics. The angle ϕ_2, or α, is defined to be $arg\left[-\frac{V_{ud}V_{ub}^*}{V_{td}V_{tb}^*}\right]$, and can be studied using neutral B decays.

B^0 mesons are not formed by a single CP eigenstate. They are a combination of CP-odd and CP-even eigenstates. B^0 and $\bar{B^0}$ can decay to a given eigenstate f, either directly or through mixing. Over time the mixing probability changes causing the decay amplitude to change. The time dependant decay rate of B^0 meson to a fianl state f is given by

$$\begin{aligned} \Gamma(B^0(t) \to f) = \;& e^{-\Gamma|t|}[(|A_f|^2 + |\bar{A_f}|^2) - (|A_f|^2 - |\bar{A_f}|^2) \\ & cos(\Delta m t) + 2|A_f|^2 Im(\lambda_f) sin(\Delta m t)] \end{aligned} \tag{2}$$

where A_f and $\bar{A_f}$ are the respective amplitudes of $B^0 \to f$ and $\bar{B}_0 \to f$, and λ_f is the mixing parameter, $e^{-\Phi_M}\frac{A_f}{A_f}$ where Φ_M is the mixing angle between B^0 and $\bar{B^0}$ 1). Once the time dependant decay rates have been measured, the CP asymmetry is calculated as $a = \frac{\Gamma(B^0 \to f) - \Gamma(\bar{B^0} \to f)}{\Gamma(B^0 \to f) + \Gamma(\bar{B^0} \to f)}$.

2 Measuring $B \to \pi^+\pi^-$

All $B \to \pi\pi$ decays proceed through the $\bar{b} \to \bar{u}u\bar{d}$ quark subprocess. $B^0 \to \pi^+\pi^-$ can proceed via the tree-level process shown in figure 1, with a branching fraction proportional to $|V_{ub}^{*2}V_{ud}^2|$. This leads to the asymmetry

$$a = \frac{1}{1+|\lambda_{+-}|^2}[(1-|\lambda_{+-}|^2)cos(\Delta mt) - 2Im\lambda_{+-}sin(\Delta mt)] \qquad (3)$$

with *sin* term $Im\lambda_{+-} = Im(e^{-\Phi_M}\frac{A_{+-}}{A_{+-}} = sin\phi_2)$ $^{1)}$.

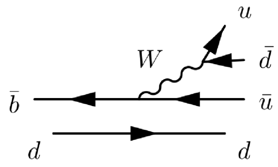

Figure 1: $B \rightarrow \pi^+\pi^-$ *proceeding through a tree process*

However, there is a second diagram through which a B^0 can decay into $\pi^+\pi^-$. This is the penguin process shown in figure 2, and in this case is expected to be comparable in magnitude to the tree process. The result is that the asymmetry does not measure $sin\phi_2$, but instead measures $sin(\phi_2 + \kappa)$.

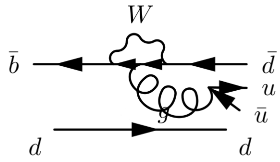

Figure 2: $B \rightarrow \pi^+\pi^-$ *proceeding through a penguin process*

3 An Isospin Analysis

In order to extract information from this measurment it is vital to subtract the penguin component of the decay amplitude. This can be achieved through the measurement from the complete $B^0 \rightarrow \pi\pi$ system, and subjecting this to an isospin analysis.

To begin, the $\pi\pi$ system is described by $\phi(\pi\pi) =| I, I_3\rangle$ with I being the isospin of the state, and I_3 is its z-projection of that isospin. The different final states are found using the Clebsh-Gordon coefficients as below

Table 1: *Relative amplitudes of* $B \to \pi\pi$.

$A(B^+ \to \pi^+\pi^0)$	$= \frac{\sqrt{3}}{2} A_{\frac{3}{2},2}$
$\frac{1}{\sqrt{2}} A(B^0 \to \pi^+\pi^-)$	$= \frac{1}{\sqrt{12}} A_{\frac{3}{2},2} - \frac{1}{\sqrt{6}} A_{\frac{1}{2},0}$
$A(B^0 \to \pi^0\pi^0)$	$= \frac{1}{\sqrt{3}} A_{\frac{3}{2},2} - \frac{1}{\sqrt{6}} A_{\frac{1}{2},0}$

$$\begin{aligned} \phi(\pi^0\pi^0) = &\quad \mid 1,0\rangle \mid 1,0\rangle = \sqrt{\tfrac{2}{3}} \mid 2,0\rangle - \sqrt{\tfrac{1}{2}} \mid 0,0,\rangle \\ \phi(\pi^0\pi^+) = &\quad \mid 1,0\rangle \mid 1,+1\rangle = \mid 2,+1\rangle \\ \phi(\pi^+\pi^-) = &\quad \mid 1,+1\rangle \mid 1,-1\rangle = \sqrt{\tfrac{1}{3}} \mid 2,0\rangle + \sqrt{\tfrac{2}{3}} \mid 0,0,\rangle \end{aligned} \tag{4}$$

At the quark level we have $\phi(B \to \bar{u}u\bar{d}) = A_{\frac{3}{2}} \mid \frac{3}{2},+\frac{1}{2}\rangle + A_{\frac{1}{2}} \mid \frac{1}{2},+\frac{1}{2}\rangle$.

The amplitudes of the isospin $\frac{3}{2}$ and $\frac{1}{2}$ components, $A_{\frac{3}{2}}$ and $A_{\frac{1}{2}}$, are the unknowns to be extracted. Finally, the initial state is $\phi(B^0) = \mid \frac{1}{2},-\frac{1}{2}\rangle$. If we apply the transition to the initial state we find

$$\begin{aligned} \phi(\bar{b} \to \bar{u}u\bar{d})\phi(B^0) &= A_{\frac{3}{2}} \mid \frac{3}{2},+\frac{1}{2}\rangle + A_{\frac{1}{2}} \mid \frac{1}{2},+\frac{1}{2}\rangle \mid \frac{1}{2},-\frac{1}{2}\rangle \\ = \sqrt{\frac{1}{2}} A_{\frac{3}{2}} \mid 2,0\rangle &+ \sqrt{\frac{1}{2}}(A_{\frac{1}{2}} + A_{\frac{3}{2}}) \mid 1,0\rangle + \sqrt{\frac{12}{A}_{\frac{1}{2}}} \mid 0,0\rangle \end{aligned} \tag{5}$$

The $\pi^0 pi^0$ final state is described in equation 6.

$$\begin{aligned} Br(B^0 \to \quad \pi^0\pi^0) &= (\sqrt{\tfrac{2}{3}}\langle 2,0 \mid -\sqrt{\tfrac{1}{2}}\langle 0,0, \mid)(\sqrt{\tfrac{12}{A}_{\frac{3}{2}}} \mid 2,0\rangle \\ &+\sqrt{\tfrac{1}{2}}(A_{\frac{1}{2}} + A_{\frac{3}{2}}) \mid 1,0\rangle + \sqrt{\tfrac{1}{2}} A_{\frac{1}{2}} \mid 0,0\rangle) \\ &= \sqrt{\tfrac{1}{3}} A_{\frac{3}{2}} + \sqrt{\tfrac{1}{6}} A_{\frac{1}{2}} \end{aligned} \tag{6}$$

This is done for all three final states, the results of which are found in table 1. For convenience two new constants are defined so that $A_0 = \sqrt{\frac{1}{6}}$ and $A_2 = \sqrt{\frac{1}{12}}$. Theses amplitudes relate to $\Delta I = 0$ and $\Delta I = 2$ respectively, and simplify the above relations to those of equation 7.

These relations can be used to form a triangle with Θ, as seen in figure 3, the angle between A_0 and A_2. In order to further constrain the system, it's observed that the penguin process can only proceed through the A_0 modes. It is a strong process, and requires isospin to be conserved. From this it can be deduced that A_2 components are purely tree processes, hence $\bar{A}_2 = e^{-2i\Phi_T} A_2$ where Φ_T is the CKM phase in the tree diagram, such that $|A^{\bar{0}+}| = |A^{0-}| = |A^{0+}|$. This tells us that the triangle with lengths equal to the conjugate processes will share a common base with the first, non-conjugate triangle. While the magnitude of both Θ and $\bar{\Theta}$, and hence $cos(\Theta)$ are determinable, the orientation of either triangle, that is to say $sin(\Theta)$ and the sign of Θ, are not.

$$A^{00} = 2A_2 + A_0 \; A^{0+} = 3A_2 \; \sqrt{\frac{1}{2}} A^{+-} = A_2 - A_0 \tag{7}$$

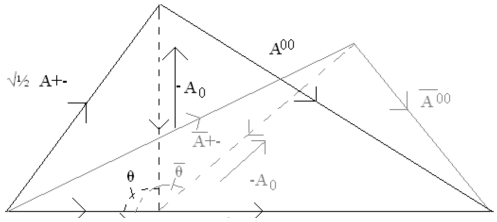

Figure 3: *The relation between A_0, A_2, $\bar{A}_0$, and $\bar{A}_2$*

λ_{+-}, the mixing parameter for $B^0 \to \pi^+\pi^-$, is $\lambda_{+-} = e^{-2i\phi_M}\frac{\bar{A}_{+-}}{A_{+-}}$. Using the relations above, and allowing $z = \frac{A_0}{A_2}$ it can be shown that 2)

$$\lambda_{+-} = e^{-2i\Phi_M}\frac{\bar{A}_2 - \bar{A}_0}{A_2 - A_0} = e^{-2i(\Phi_M + \Phi_T)}\frac{1-\bar{z}}{1-z} = e^{-2i\phi_2}\frac{1-|\bar{z}|e^{\pm i\bar{\Theta}}}{1-|z|e^{\pm i\Theta}} \tag{8}$$

The $\pm\Theta$ term is the result of the ambiguity discussed above. The same process applied to $B^0 \to \pi^0\pi^0$ yields $\lambda_{00} = e^{-2i\phi_2}\frac{1-\frac{1}{2}|\bar{z}|e^{\pm i\bar{\Theta}}}{1-\frac{1}{2}|z|e^{\pm i\Theta}}$. The angle ϕ_2 is related to Θ in the following way

$$sin(2\phi_2 + \kappa_{00}) = Im(\lambda_{00})|\frac{1 - \frac{1}{2}|z|e^{\pm 2i\Theta}}{1 - \frac{1}{2}|\bar{z}|e^{\pm 2i\bar{\Theta}}}| \tag{9}$$

$$sin(2\phi_2 + \kappa_{+-}) = Im(\lambda_{+-})|\frac{1 - |z|e^{\pm 2i\Theta}}{1 - |\bar{z}|e^{\pm 2i\bar{\Theta}}}| \tag{10}$$

where κ is the penguin pollution in each process. Each of equations 9 and 10 have four solutions for ϕ_2. The solutions that overlap between the two equations determine ϕ_2 if individual measurements of A_{00}, $\bar{A_{00}}$, A_{+-}, and $\bar{A_{+-}}$ are availible, However, this can be experimentally difficult, as it's difficult to distinguish $B^0 \rightarrow \pi^0\pi^0$ from $\bar{B}^0 \rightarrow \pi^0\pi^0$. In the case that this is not possible, or if there is overlap between 2 values of ϕ_2 from the two decay channels, there will be an element of ambiguity left in the measurment of ϕ_2.

Instead, it is possible to find an upper bound on on the size of the penguin polution, κ. In this case the diagram in figure 3 is redrawn to assume maximise the contributions of Θ and $\bar{\Theta}$. This occurs when $A_{00} = \bar{A_{00}}$, 3) and so $\bar{\Theta} = \Theta$. When this constraint is applied, $sin^2(\kappa_{00}) \leq \frac{A_{00} + \bar{A_{00}}}{A_{0-} + A_{0+}}$.

4 Conclusion

The measurements of $B^0 \rightarrow \pi^0\pi^0$ and $\bar{B}^0 \rightarrow \pi^0\pi^0$ are vital for an improve the measurement of ϕ_2. However, an improving the measurment of the combined amplitude of $B^0\bar{B}^0 \rightarrow \pi^0\pi^0$ will still lead to an improved upper bound on the penguin pollution.

References

1. Lipkin, H. J. *et al*, Phys. Rev. D. **44**, 1454 (1991).
2. Gronau, M. *et al*, Phys. Rev. Lett. **65**, 3381 (1990).
3. Grossman, Y. *et al*, Phys. Rev. D. **58**, 017504 (1998).

Frascati Physics Series Vol. XLVIII (2009), pp. 73-78
Young Researchers Workshop: *"Physics Challenges in the LHC Era"*
Frascati, May 11 and 14, 2009

A MICROCALORIMETER MEASUREMENT OF THE NEUTRINO MASS, STUDYING ^{187}Re SINGLE β DECAY AND ^{163}Ho ELECTRON-CAPTURE DECAY

Daniela Bagliani
University and INFN of Genoa, Italy

Abstract

The neutrino mass scale is a relevant parameter of the theoretical framework beyond the Standard Model of particle physics, and therefore a crucial challenge of future experimental efforts. In this paper I will make an overview of the proposals for the direct searches of the absolute neutrino mass by means of ^{187}Re single β decay and ^{163}Ho electron-capture decay. The sensitivity, needed to constrain m_ν, is achieved thanks to the high responsivity of superconducting microcalorimeters and their low intrinsic noise.

1 Introduction

In the Standard Model framework neutrino mass scale represent an open problem whose solution could provide crucial informations in Cosmology, Particle and Astroparticle Physics. Because neutrino are massive, single β

decay and neutrinoless double-β-decay could set the absolute scale and nature, Dirac or Majorana.

Presently, the lower limits on electron neutrino mass (2.2 eV) have come from tritium β-decay experiments. The aim of these experiments is the analysis of the events near the endpoint energy, where the spectral shape is affected by the modifications of the phase-space factor induced by a finite neutrino mass. Calorimetric techniques have been developed in the past few years with the aim to achieve higher sensitivity and lower systematics than in well-established β-impulse spectroscopy.

2 Calorimetric measurement of ^{187}Re single β decay and ^{163}Ho electron-capture decay

The measurement of the neutrino mass via single β and electron capture (EC) decays is done by searching the deficit at the end-point of energy spectrum. The deficit amplitude in both cases scales as the third power of the neutrino mass. The required high sensitivity in the 0.1 eV/c^2 region makes ^{187}Re and ^{163}Ho decays favourite candidates for calorimetric spectroscopy, due to their low endpoints: 2.5 keV for ^{187}Re, and $2.5 \div 2.8$ keV for ^{163}Ho.

2.1 ^{187}Re single β decay

Natural metallic rhenium is composed by ^{187}Re for its 63%. ^{187}Re decays in ^{187}Os, and the whole energy released can be measured detecting the temperature rise following the absorption of the emitted electron by the rhenium crystal itself cooled at 0.1 K 1).

This is the principle of operation of the calorimetric spectroscopy for rhenium β decay, that offers several advantages. The decay energy spectrum can directly be measured, without model dependent corrections for atomic and molecular final states. Nuclear recoil energy and electron energy losses don't affect the spectrum shape. Unfortunately rhenium decay is first forbidden unique: the ^{187}Re half life is 4.5×10^{10} years, thereby the specific count rate is very low. The expected activity of 1 mg is 1 Bq.

2.2 ^{163}Ho electron-capture decay

Holmium EC decay is a promising alternative tool respect to the study of rhenium [2]. The first advantage is the holmium half life: 4.5×10^3 years. The EC energy spectrum has a shape for finite m_ν very similar to the rhenium decay at the endpoint, but the half life seven order shorter can significantly improve the statistics. Moreover the EC spectrum presents lines corresponding to the inner orbitals M and N involved in the process, consequently the source can be even employed for self calibration of the microcalorimeter, monitoring its linearity during the measurements.

Despite all, the study of ^{163}Ho require a technological effort in assembling the source. ^{163}Ho in metallic state must be produced in laboratories and embedded into an adequate absorber. The modern techniques of producing beams of heavy ions allow to obtain ^{163}Ho by fragmentation or spallation of atoms in a target hit by protons, as in the ISOLDE facility at the CERN laboratories. The beam of resulting products could implant ^{163}Ho in a layer less than 1 μm thick. Much care must be taken for the purification process from isobars, which could contaminate the source with excess radioactivity.

3 The superconducting microcalorimeters

In the last two decades thermal detectors have developed reaching the highest sensitivity available at keV energies. Here we consider a specific kind of detectors, the transition edge sensor (TES) microcalorimeters. These cryogenic detectors have been employed to study electromagnetic radiation from X-rays to the far infrared in many different physics domains, reporting an energy resolution up to two order of magnitude better than most performing solid state detectors off the shelf.

In first approximation we can describe the microcalorimeter in three fundamentals elements: an absorber of heat capacity C strongly thermally coupled to a sensor, the sensor itself and a weak thermal link of conductance G coupled to an heat sink. At each radiation absorption the detector response is a temperature transient $\Delta T = E_R/C$, where E_R is the energy absorbed. The initial temperature is restored fastly by the help of the electrothermal feedback (ETF) with a time scale $\tau = C/(G - G_{ETF})$.

To take the advantage of fast pulses produced by ETF, TES are made of a superconducting thin film biased with a constant voltage and it is cooled at a working temperature corresponding to an electrical resistance of a few percents of the normal value. The whole sensitivity of these detectors is related to the steepness of the phase transition. If the film is patterned and has an inner structure with low impurities, the transition width can be as narrow as 0.3 mK, giving very high temperature responsivity. Thermal fluctuations due to Brownian motion of phonons in the film represent the intrinsic energy resolution of the TES. Their root mean square amplitude can be estimated as $\Delta U_{rms} = \sqrt{k_B T^2 C}$. The resulting achievable energy resolution is $\Delta E_{FWHM} = \zeta\sqrt{k_B T^2 C}$, that in a typical case is less than 1 eV. The parameter ζ contains the dependence from the ETF, G and the steepness of the transition. For further details on TES thermal and electrical models see ref. $^{3)}$.

In the Genoa Laboratories we produce TES of thin Ir/Au bilayers, with Al electrical contacts. Iridium films are grown on a $\mathrm{Si}_x\mathrm{N}_y$ membrane by pulsed laser deposition. Gold is evaporated by electron gun on an Ir sticking layer a few angstroms thick, which provide strong film adhesion to the substrate. Finally the Ir film is deposited on the top of the gold layer. The Ir/Au bilayer is fabricated in ultra high vacuum chambers connected between them. Typical thicknesses are from 50 to 100 nm for Ir films, and 20 to 50 nm for Au layers. Thin films patterning is performed by microlithography in a clean room and dc sputtering. Typical final geometry of the TES is a rectangular shape of $100 \times 120\ \mu\mathrm{m}^2$. The characterization measurements of our films have shown transition temperatures between 100 and 120 mK at constant currents between 50 nA and 1 μA. The transition width is of fractions of millikelvin and normal state resistance is of some tenths of Ohm.

The absorber preparation consist of two different processes for rhenium and holmium. In the first case a pure Re crystal of cubic shape is cut and optically lapped in order to obtain an homogeneous superconductivity state at the working temperature. Re become superconductive at 1.7 K and according to the BCS theory its thermal capacitance is strongly suppressed in the superconducting state; thereby single crystal fabrication is a crucial phase of the calorimeter fabrication, being the Re the bigger contribute to the total sensor capacitance and consequently its energy resolution. The crystal is then fixed on the TES with epoxy glue.

Holmium absorber must be composed of two parts: a superconducting absorber layer (i.e. Bi, Sn) where the Ho atoms are implanted, and a thicker layer covering the implanted area for the absorption of the secondary products of EC decay (emission of X-rays and Auger electrons, Coster-Kronig transitions). For a full absorption of the whole decay energy and for stopping efficiently the implantation beam the absorber should be a few microns thick. In figure 1 we describe the rhenium and holmium microcalorimeters.

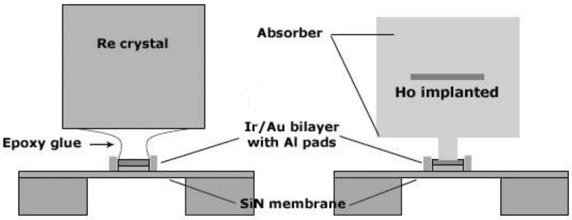

Figure 1: *Scheme of the two microcalorimeters; the second one has an absorber grown on the sensor with an inner layer containing atoms of* ^{163}Ho *homogeneously implanted.*

4 SQUID amplifier for TES arrays

The sensitivity that we foresees to achieve is $0.1 \div 0.3$ eV/c^2 with a statistics of $10^{12} \div 10^{14}$. The energy resolution of one microcalorimeter with 1 mg of Re at keV energies can be of few eV, but the quest of such high statistics makes necessary to fabricate arrays of several elements in order to have 5 years data taking. The purpose of the MARE collaboration (Microcalorimeters Array for Rhenium Experiments) is to assemble arrays for a total of 50000 detectors, and a final sensitivity of 0.2 eV. Being TES low impedance devices, the readout should be a frequency multiplexed SQUID amplifier 4). A simple example of the cryogenic stage of the readout is reported in the figure 2. The scheme is composed by a set of resonating circuits associated to each TES. Each sensor is biased at different frequencies. the signals of a row of TES are summed in a single channel and can be read by a single SQUID. By this way a row can contain tens of detectors.

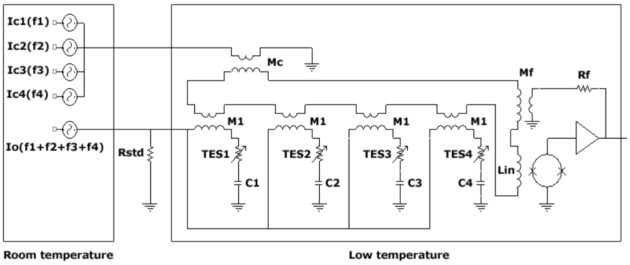

Figure 2: *The readout circuit is composed by a room temperature stage and another one cooled at the working temperature, typically below* 0.1 *mK.*

5 Conclusions

A calorimetric measurements of the neutrino mass with a sensitivity of 0.2 eV should be possible, thanks to the high sensitivity of TES microcalorimetry. A prototype of cryogenic electronics is under study in our laboratories and we foresee to test a first array of Re microcalorimeters in the next runs.

References

1. F. Gatti *et al*, Nucl. Instr. and Meth. in Phis. Res. A **315**, 260 (1992).
2. F. Gatti *et al*, J. Low. Temp. Phys. **151**, 603 (2008).
3. K.D. Irwin and G.C. Hilton, *Cryogenic Particle detection* edited by Springer **99**, 63 (2005)
4. R. Vaccarone, J. Low. Temp. Phys. **151**, 915 (2008).

Frascati Physics Series Vol. XLVIII (2009), pp. 79-84
Young Researchers Workshop: *"Physics Challenges in the LHC Era"*
Frascati, May 11 and 14, 2009

MEASUREMENT OF THE ANTIPROTON/PROTON RATIO AT FEW-TeV ENERGIES WITH THE ARGO-YBJ EXPERIMENT

Roberto Iuppa
INFN, Sezione Roma Tor Vergata
Dipartimento di Fisica, Università Roma di Tor Vergata
on behalf of the ARGO-YBJ collaboration

Abstract

Cosmic rays are hampered by the Moon, therefore a deficit of cosmic rays in its direction is expected (the so-called *Moon shadow*). The Earth-Moon system acts as a magnetic spectrometer and the paths of primary protons and antiprotons are deflected in an opposite sense in their way to the Earth. This effect allows, in principle, the search of antiparticles in the opposite direction of the observed Moon shadow. Cosmic ray antiprotons provide an important probe for the study of cosmic-ray propagation in the interstellar space and to investigate the existence of Galactic dark matter.

With the data of the ARGO-YBJ experiment, an upper limit of the $\bar{p}/p$ fluxes ratio in the few-TeV energy region is set to a few percent with a confidence level of 90%.

1 Introduction

The study of cosmic ray (CR) antiprotons might allow to investigate the baryonic asymmetry of the universe and to uncover evidence for the existence of galactic dark matter. Altough recent measurements up to about 100 GeV [1, 2, 3] are consistent with the conventional CR model, in which antiprotons are secondary particles yielded by the spallation of CR nuclei over the interstellar medium, exotic models of primary $\overline{p}$ production not ruled out by low energy measurements are available. Some scenarios provide a $\overline{p}/p$ ratio increasing up to the 10% level in the few-TeV energy range [4].

Furthermore, cosmic ray antiprotons, as well as positrons, are considered as prime targets for indirect detection of galactic dark matter [5]. As an example, some recent analyses suggest that the overall PAMELA [3, 6] $\overline{p}$ and e^+ data and ATIC/PPB-BETS [7, 8] $e^+ + e^-$ data can be reproduced taking into account a heavy DM particle (M $\geq$10 TeV) that annihilates into W^+W^- or hh [9]. Also in this case, the $\overline{p}/p$ ratio reaches the 10^{-2} level in the TeV energy region.

The geomagnetic field should deflect the antimatter component of the cosmic rays in the opposite direction with respect to the matter one. Therefore, the Moon or Sun shadows can be used as charge spectrometer to measure the cosmic ray antiprotons abundance exploiting the separation of the proton and antiproton shadows [10]. Nonetheless, there is an optimal energy window for the measurement of the antiprotons abundance. At high energy ($\geq$ 10 TeV) the magnetic deflection is too small compared to the angular resolution and the shadows cannot be disentangled. At low energy ($\approx$100 GeV) the well separated shadows are washed out by the poor angular resolution, thus limiting the sensitivity.

In this paper we report on the measurement of the $\overline{p}/p$ ratio in the few-TeV energy region exploiting the observation of the galactic cosmic ray Moon shadowing effect performed by the ARGO-YBJ experiment.

2 The ARGO-YBJ experiment

The ARGO-YBJ detector, located at the YangBaJing Cosmic Ray Laboratory (Tibet, P.R. China, 4300 m a.s.l.), is the only experiment exploiting the *full coverage* approach at very high altitude. The detector is constituted by a central carpet ~74×78 m^2, made of a single layer of Resistive Plate Chambers (RPCs) with ~92% of active area, enclosed by a partially instrumented guard ring that extends the detector surface up to ~100×110 m^2, for a total active surface of ~6700 m^2. The apparatus has a modular structure, described in 11).

The spatial coordinates and the time of any detected particle are used to reconstruct the position of the shower core and the arrival direction of the primary 12).

The ARGO-YBJ experiment started recording data with the whole central carpet in June 2006. Since 2007 November the full detector is in stable data taking (trigger particles multiplicity N_{trig} =20) with a duty cycle ~ 90%: the trigger rate is about 3.6 kHz.

3 Monte Carlo Simulation

The air showers development in the atmosphere has been generated with the CORSIKA v.6.500 code including the QGSJET-II.03 hadronic interaction model for primary energy above 80 GeV and the FLUKA code for lower energies 13). Cosmic ray spectra of p, He and CNO have been simulated in the energy range from 30 GeV to 1 PeV following 14). About $3{\cdot}10^{11}$ showers have been distributed in the zenith angle interval 0-60 degrees. The secondary particles have been propagated down to a cut-off energy of 1 MeV. The experimental conditions have been reproduced via a GEANT3-based code. The shower core positions have been randomly sampled in an energy-dependent area up to $10^3 \times 10^3$ m^2, centered on the detector.

A detailed Monte Carlo simulation of cosmic rays propagation in the Earth-Moon system has been developed to compare the observed displacement of the shadow with the expectations, so disentangling the effect of the geomagnetic field from a possible systematic pointing error.

4 Data analysis

For the analysis of the shadowing effect a $10^\circ \times 10^\circ$ sky map in celestial coordinates with $0.1^\circ \times 0.1^\circ$ bin size, centered on the Moon location, is filled with the detected events. The background is evaluated with the so-called *time swapping* method as described in 15).

To form conservative estimate of the $\bar{p}/p$ ratio in this preliminary work the

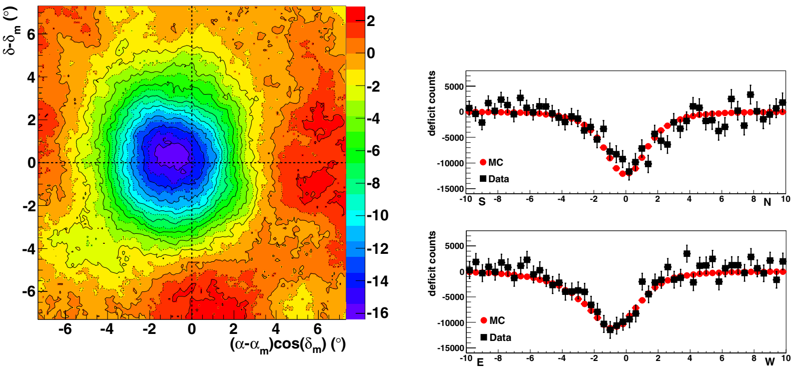

(a) (b)

Figure 1: *a) Moon shadow observed by the ARGO-YBJ experiment. The color scale gives the statistical significance. b) Upper (lower) panel: deficit counts observed around the Moon projected along the North-South (East-West) axis for N= 30-60 (black squares) compared to the MC simulation expectations.*

analysis refers to about $6 \cdot 10^8$ events collected only during the stable operation period of data taking after the following event selection: (1) particle multiplicity on the central carpet $N > 30$, to avoid any threshold effect; (2) the zenith angle of the event arrival direction should be less than 50°; (3) the reconstructed core position should be inside an area 250×250 m^2 around the detector; (4) the reduced χ^2 of the final temporal fit should be less than 100. A significance map of the Moon shadow is shown in Fig. 1(a). It contains all the events belonging to the lowest multiplicity bin investigated (N = 30-60), collected by ARGO-YBJ during the period December 2007 - December 2008 (1350 hours on-source). The sensitivity of the observation is about 17 standard deviations and the Moon is shifted westward by about 1°. This means that a potential antiproton signal is expected eastward within 1.5° from the actual Moon position. The median energy of selected events is $E_{50} \approx 1.4$ TeV (mode energy $\sim$ 0.30 TeV) for proton-induced showers. The corresponding angular resolution is $\sim$1.8°.

The projection along the North-South (East-West) direction of the deficit counts around the Moon is shown in the upper (lower) panel of Fig. 1(b) for N = 30-60, together with the MC expectations. The vertical axis reports the events contained in an angular projection parallel to the North-South (East-

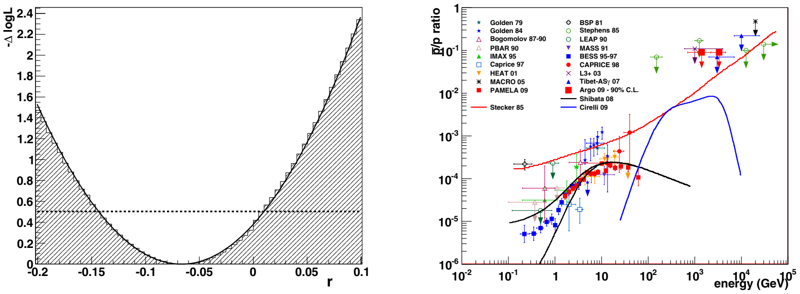

(a) (b)

Figure 2: *a) $\Delta log\mathcal{L}$ as a function of r (the ($\bar{p}$) content) for N = 30-60. The dashed line $\Delta log\mathcal{L}$ = 0.5 is used to determine the 68.3% central confidence level. b) The antiproton to proton flux ratio obtained with the ARGO-YBJ experiment compared with all available measurements.*

West) axis and centered to the observed Moon position. The width of this band is ±3.3°. Since at the Yangbajing latitude the effect of the geomagnetic field along the North-South direction is negligible, a nearly symmetrical and centered projection is expected.

5 Results and discussion

In order to evaluate the $\bar{p}/p$ ratio, a maximum likelihood fit of the experiment data to the MC expectations has been performed using the $\bar{p}$ content as a free parameter. It has been done for two different multiplicity bins: N = 30-60 and N>60. From the MC simulation it results that the median energy of all selected events is E_{50} = 1.85 TeV for N = 30-60 and E_{50} = 4.10 TeV for N>60.

The result is shown in Fig. 2(a) for N = 30-60 and one finds $r_{min} = \Phi(\bar{p})/\Phi(mat) = -0.065 \pm 0.078$, which is below a physical boundary (the $\bar{p}$ content must be positive). An upper limit of 7.4% with 90% confidence level is set for N = 30-60. For higher multiplicities (N>60) an upper limit of 7.4% is set with 90% c.l.. By correcting for the protons abundance within the CR, these limits correspond to a $\bar{p}/p$ ratios of 0.09 for N = 30-60 with 90% c.l. and 0.09 for N> 60 with 90% c.l., respectively. In Fig. 2(b) the ARGO-YBJ results are shown with a compilation of the available measurements [16]. The solid curve refers to a direct production model, the dashed line refers to a model of primary $\bar{p}$ production by antistars $^{4)}$ and the dotted one refers to the contribution of an heavy DM particle $^{9)}$.

6 Conclusions

The ARGO-YBJ experiment is observing the Moon shadow with high statistical significance. Using about 1 year data, a preliminary upper limit of the $\bar{p}/p$ flux ratio is set to 0.09 with a confidence level of 90% at a median energy of 1.85 and 4.10 TeV.

References

1. A. Yamamoto et al., *Nucl. Phys. B Proc. Suppl.* **166B** (2007) 62.
2. M. Boezio et al., *ApJ* **561** (2001) 787.
3. O. Adriani et al., *Phys. Rev. Lett.* **102** (2009) 051101.
4. S.A. Stephen and R.L. Golden, *Space Sci. Rev.* **46** (1987) 31.
5. F. Donato et al., *Phys. Rev. Lett.* **102** (2009) 071301.
6. O. Adriani et al., *Nature* **458** (2009) 607.
7. J. Chang et al., *Nature* **456** (2008) 362.
8. K. Yoshida et al., *Adv. in Space Res.* **42** (2008) 1670.
9. M. Cirelli et al., *hep-ph/0809.2409v3* (2008) and *hep-ph/0903.3381* (2009).
10. J. Linsley, *Proc. 19th ICRC* **3** (1985) 465.
11. G. Aielli et al., *NIM* **A562** (2006) 92.
12. G. Di Sciascio et al., *Proc. 30th ICRC* (2007) (preprint: arXiv:0710.1945).
13. D. Heck et al., Report **FZKA 6019** (1998).
14. B. Wiebel-Sooth et al., *A&A* **330** 389, 1998.
15. D. E. Alexandreas et al., *NIM A* **328** (1993) 570.
16. M. Amenomori et al., *Astrop. Phys.* **28** (2007) 137 and reference therein.

Frascati Physics Series Vol. XLVIII (2009), pp. 85-90
Young Researchers Workshop: *"Physics Challenges in the LHC Era"*
Frascati, May 11 and 14, 2009

EVENT RECONSTRUCTION IN THE DRIFT CHAMBER OF THE CMD-3 DETECTOR

A.V. Karavdina*
Budker Institute of Nuclear Physics, Novosibirsk, Russia

Abstract

Charged particles tracks and vertex reconstruction as well as offline-calibrations in the drift chamber of the CMD-3 detector are described. Event reconstruction algoritm was tested on simulation in the magnetic field. Spatial resolution $90\div120$ μm in the drift plane and $1.5\div3$ mm along wires were obtained in test experiments without the magnetic field.

1 Introduction

The new electron-positron collider VEPP-2000 1) is being now under commissioning at Budker Institute of Nuclear Physics. Using round beams technique the collider will provide the luminosity up to 10^{32} cm^{-2}s^{-1} at the maximum

---

[*] On behalf of the CMD-3 Collaboration

c.m. energy $\sqrt{s} = 2$ GeV. Main goals of experiments at the VEPP-2000 are studies interaction of light quarks produced in e^+e^- collisions, test of existing theoretical and phenomenological models and provide precise information for future models. It requires a detector with high efficiency for multypartice events and good energy and angular resolutions for charged particles as well as for photons.

Two modern detectors, a general purpose detector CMD-3 (Cryogenic Magnetic Detector) and SND (Spherical Neutral Detector), will be installed in the two interaction regions of the collider. The CMD-3 detector consists of a cylindrical drift chamber and Z-chamber inside thin ($0.18X_0$) superconductive solenoid with the 1.35 T magnetic field, end-cap BGO calorimeter, barrel liquid xenon and CsI calorimeters, TOF counters between LXe and CsI calorimeters and cosmic veto counters. In more detail the CMD-3 detector is described elsewhere 2).

2 Drift chamber

The drift chamber is a cylinder of 44 cm length and 60(4) cm outer(inner) diameter. The sensitive volume of the drift chamber is filled by 1218 identical hexagonal drift cells. The cell side length is 9 mm. Each sense wire is surrounded by 6 field wires. Charge division technique is used to measure coordinate along sense wires which have 15 μm diameter and are made of gold plated tungsten-rhenium alloy with resistance of 1 kΩ/m. Field wires have 100 μm diameter and are made of titanium. The drift chamber is filled with a 80:20 mixture of argon and isobutane. In more detail the drift chamber construction is discussed elsewhere 3).

The digitized measurements of time and two charges from the ends of sense wires are provided by T2Q boards that were produced at the Institute workshop. Analog and digital parts of it are placed on one board. The board is made in BigCAMAC standard and serves 16 sense wires.

3 Track reconstruction

Direct measurements of the magnetic field in the drift chamber volume have shown good agreement with calculations. The maximum deviation of the z-component of the magnetic field does not exceed 1% along the beam axis and

0.2% from the interaction point to the outer shell. Due to high uniformity of the magnetic field the helix based track approximation is used in the reconstruction. Five parameters essential for the helix description are shown in Fig. 1.

The track reconstruction chain consists of several stages. The first one is a pattern recognition to select track candidates and to obtain the first approximation of the track parameters based on the histogramming method. We assume the impact parameter is equal to zero and use the two-dimensional histogramming method separately in the (k-φ) and (z-θ) planes.

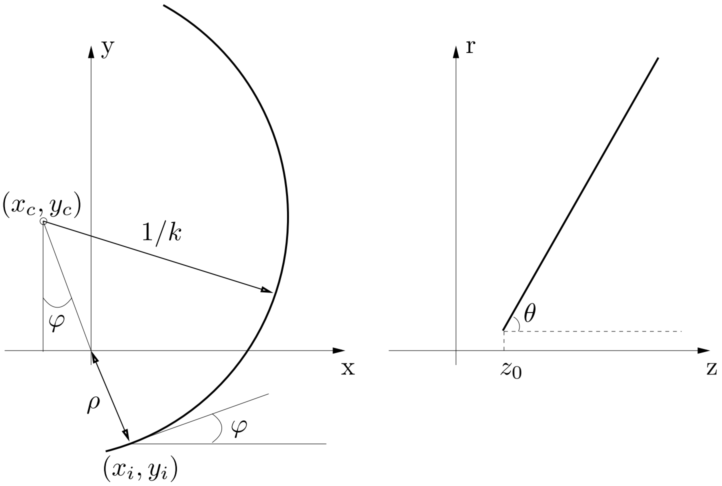

Figure 1: *Track parameters: k is a curvature of the track; φ, θ are angles; z_0 is a coordinate of the track origin on the z axis and ρ is an impact parameter (the shortest distance between the beam line and the track projection on the (x, y) plane).*

If number of cells associated to a track-candidate is more than five, such candidate for a track is used in approximation. In the track fit we use the least-squares method and obtain parameters of the track with the covariance matrix. After the track fit we try to add nearby cells to the track.

When all tracks in the event were reconstructed we check quality of associated cells in the track. For right association cells to the track contribution of each hit in the chi-square of each track is calculated. And for its own track hit must give the least contribution to chi-square. This algorithm allows us to reconstruct high mulitplicity events with close tracks.

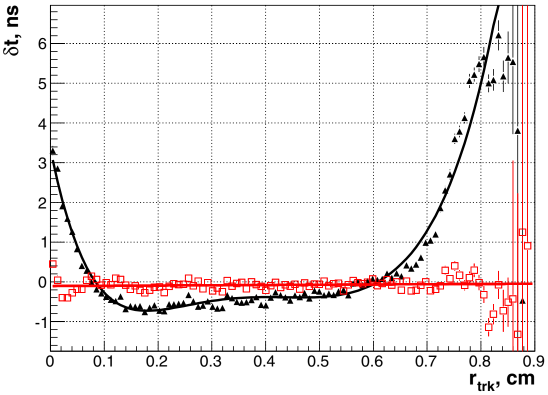

Figure 2: *Time residuals (triangles – before calibration, squares – after calibrations).*

4 Offline calibration

To reconstruct a coordinate in a cell we use time dependence $t(r, \varphi)$ on the distance from wire to the track and the φ angle in the cell. Due to the hexagonal structure of the drift chamber all cells are identical and have the same space-time relation $t(r, \varphi)$ initially got from Garfield. A calibration technique has been developed to improve spatial resolution using experimental data. Correction shown in Fig. 2 is obtained as time residual, which is function of a radius and an angle in a cell. The improvement of resolution in the perpendicular plane after the offline calibration of space-time relation is shown in Fig. 3.

To improve resolution in the z-coordinate residuals between the measured in cell z-coordinate and the fitted z-coordinate of the track are minimized by using the least-squares method. Parameters of the minimization are length of wire, pedestals, gain and input impedances of the T2Q channels. Dependence of resolution on the track z-coordinate is shown in Fig. 3.

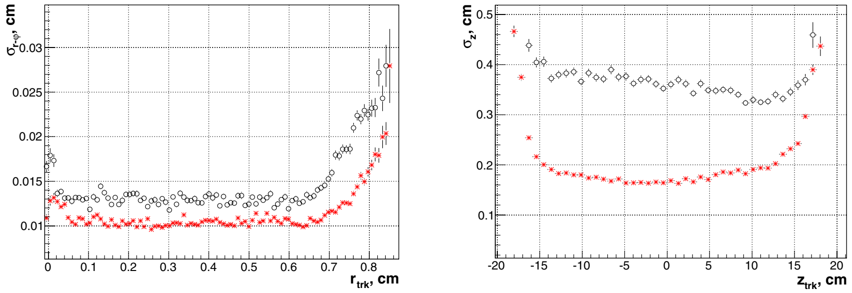

Figure 3: *a) Resolution in the r-ϕ-plane versus distance to a sense wire; b) Resolution of the z-coordinate (circles – before calibration, stars – after calibration).*

5 Vertex Reconstruction

The vertex reconstruction chain also consists of several stages. To search the candidate for a vertex we use a intersection of pair of tracks. Distance between the vertex-candidate and each track must be less than 5 mm. The vertex fit is performed using the tracks parameters with the covariance matrix. In the vertex fit distances between the vertex and each track in the perpendicular plane as well as along wires are minimized by the least-squares method. If the final vertex chi-square is less than χ^2_v threshold we try to add new tracks to the vertex. Otherwise the track given the largest contribution to the vertex chi-square is removed and the vertex fit procedure is repeated.

Program for the vertex reconstruction was tested on simulation. The vertex search efficiency for events with four tracks is 89%, this was tested on simulation $e^+e^- \to 2\pi^+2\pi^-$. The vertex resolution about 130 μm was obtained.

To test the vertex reconstruction algorithm on events with the vertex outside interaction region simulation of events $e^+e^- \to K_S K_L$ with decay of $K_S \to \pi^+\pi^-$ was used and invariant mass of K_S was reconstructed. From kinematic fit with vertex constrain the $\pi^+\pi^-$ invariant mass resolution about 0.5 % was obtained. It's worth to note that our simulation does not have any electronic noise and in real experiment the resolution may change.

6 Conclusion

Event reconstruction in the drift chamber of the CMD-3 detector is implemented. This software includes reconstruction of charged particles tracks, vertices and several offline calibrations. The algorithm of the track reconstruction and the offline calibrations were tested on the experimental data without the magnetic field as well as on simulation in presence of the magnetic field. The experimental resolution $90 \div 120$ μm in the perpendicular plane and $1.5 \div 3$ mm along wires was reached. The vertex reconstruction was tested on non-central ($K_S \to \pi^+\pi^-$) and central ($e^+e^- \to 2\pi^+2\pi^-$) simulated events in the magnetic field.

Test of the event reconstruction efficiency are still in progress. Also we plan to use the Kalman filter for low-energy particle track reconstruction. This method allows us taking into account multiple scattering in the track fit, which is necessary for charged kaons at the threshold.

References

1. Yu.M. Shatunov *et al.*, Proc. of EPAC 2000, 439 (Vienna, Austria, 2000).
2. G.V. Fedotovich, Nucl. Phys. B**162**, 332 (2006).
3. A. Popov *et al.*, Nucl. Instr. and Meth. A**598**, 105 (2009).

Frascati Physics Series Vol. XLVIII (2009), pp. 91
YOUNG RESEARCHERS WORKSHOP: *"Physics Challenges in the LHC Era"*
Frascati, May 11 and 14, 2009

KAONIC ATOMS AT DAΦNE

Shinji Okada
Laboratori Nazionali di Frascati dell'INFN,
Via Enrico Fermi 40, 00044 Frascati, Italy

Written contribution not received

FRASCATI PHYSICS SERIES VOLUMES

Volume I
Heavy Quarks at Fixed Target
Eds.: S. Bianco and F.L. Fabbri
Frascati, May 31–June 2, 1993
ISBN—88–86409–00–1

Volume II – Special Issue
Les Rencontres de Physique de la Vallée d'Aoste –
Results and Perspectives in Particle Physics
Ed.: M. Greco
La Thuile, Aosta Valley, March 5 –11, 1995
ISBN—88–86409–03–6

Volume III
Heavy Quarks at Fixed Target
Ed.: B. Cox
University of Virginia, Charlottesville
October 7–10, 1994, 11
ISBN—88–86409–04–4

Volume IV
Workshop on Physics and Detectors for DAΦNE
Eds.: R. Baldini, F. Bossi, G. Capon, G. Pancheri
Frascati, April 4–7, 1995
ISBN—88–86409–05–2

Volume V – Special Issue
Les Rencontres de Physique de la Vallée d'Aoste –
Results and Perspectives in Particle Physics
Ed.: M. Greco
La Thuile, Aosta Valley, March 3–9, 1996
ISBN—88–86409–07–9

Volume VI
Calorimetry in High Energy Physics
Eds.: A. Antonelli, S. Bianco, A. Calcaterra, F.L. Fabbri
Frascati, June 8–14, 1996
ISBN—88–86409–10–9

Volume VII
Heavy Quarks at Fixed Target
Ed.: L. Kőpke
Rhinefels Castle, St. Goar, October 3–6, 1996
ISBN—88–86409–11–7

Volume VIII
ADONE a milestone on the particle way
Ed.: V. Valente 1997
ISBN—88–86409–12–5

Volume IX – Special Issue
Les Rencontres de Physique de la Vallée d'Aoste –
Results and Perspectives in Particle Physics
Ed.: M. Greco
La Thuile, Aosta Valley, March 2–8, 1997
ISBN–88–86409–13–3

Volume X
Advanced ICFA Beam Dynamics
Workshop on Beam Dynamics Issue for e^+e^- *Factories*
Eds.: L. Palumbo, G. Vignola
Frascati, October 20–25, 1997
ISBN—88–86409–14–1

Volume XI
Proceedings of the XVIII International Conference on
Physics in Collision
Eds.: S. Bianco, A. Calcaterra, P. De Simone, F. L. Fabbri
Frascati, June 17–19, 1998
ISBN—88–86409–15–X

Volume XII – Special Issue
Les Rencontres de Physique de la Vallée d'Aoste –
Results and Perspectives in Particle Physics
Ed.: M. Greco
La Thuile, Aosta Valley, March 1–7, 1998
ISBN—88–86409–16–8

Volume XIII
Bruno Touschek and the Birth of thee$^+e^-$
Ed.: G. Isidori
Frascati, 16 November, 1998
ISBN—88–86409–17–6

Volume XIV – Special Issue
Les Rencontres de Physique de la Vallée d'Aoste –
Results and Perspectives in Particle Physics
Ed.: M. Greco
La Thuile, Aosta Valley, February 28–March 6, 1999
ISBN—88–86409–18–4

Volume XV
Workshop on Hadron Spectroscopy
Eds.: T. Bressani, A. Feliciello, A. Filippi
Frascati, March 8 2 1999
ISBN—88–86409–19–2

Volume XVI
Physics and Detectors for DAΦNE
Eds.: S. Bianco, F. Bossi, G. Capon, F.L. Fabbri,
P. Gianotti, G. Isidori, F. Murtas
Frascati, November 16 –19, 1999
ISBN—88–86409–21–4

Volume XVII – Special Issue
Les Rencontres de Physique de la Vallée d'Aoste –
Results and Perspectives in Particle Physics
Ed.: M. Greco
La Thuile, Aosta Valley, February 27 March 4, 2000
ISBN—88–86409–23–0

Volume XVIII
LNF Spring School
Ed.: G. Pancheri
Frascati 15–20 May, 2000
ISBN—88–86409–24–9

Volume XIX
XX Physics in Collision
Ed.: G. Barreira
Lisbon June 29–July1st. 2000
ISBN—88–86409–25–7

Volume XX
Heavy Quarks at Fixed Target
Eds.: I. Bediaga, J. Miranda, A. Reis
Rio de Janeiro, Brasil, October 9–12, 2000
ISBN—88–86409–26–5

Volume XXI
IX International Conference on Calorimetry in High Energy Physics
Eds.: B. Aubert, J. Colas, P. Nédélec, L. Poggioli
Annecy Le Vieux Cedex, France, October 9–14, 2000
ISBN—88–86409–27–3

Volume XXII – Special Issue
Les Rencontres de Physique de la Vallée d'Aoste – Results and Perspectives in Particle Physics
Ed.: M. Greco
La Thuile, Aosta Valley, March 4–10, 2001
ISBN—88–86409–28–1

Volume XXIII
XXI Physics in Collision
Ed.: Soo–Bong Kim
Seoul, Korea, June 28 30, 2001
ISBN—88–86409–30–3

Volume XXIV
International School of Space Science – 2001 Course on: Astroparticle and Gamma–ray Physics in Space
Eds.: A. Morselli, P. Picozza
L'Aquila, Italy, August 30 September 7, 2000
ISBN—88–86409–31–1

Volume XXV
TRDs for the 3rd Millennium Workshop on
Advanced Transition Radiation Detectors for
Accelerator and Space Applications
Eds. N. Giglietto, P. Spinelli
Bari, Italy, September 20–23, 2001
ISBN—88–86409–32–X

Volume XXVI
KAON 2001 International Conference on CP Violation
Eds.: F. Costantini, G. Isidori, M. Sozzi
Pisa Italy, June 12th 17th, 2001
ISBN—88–86409–33–8

Volume XXVII – Special Issue
Les Rencontres de Physique de la Vallée d'Aoste –
Results and Perspectives in Particle Physics
Ed.: M. Greco
La Thuile, Aosta Valley, March 3–9, 2002
ISBN—88–86409–34–6

Volume XXVIII
Heavy Quarks at Leptons 2002
Eds.: G. Cataldi, F. Grancagnolo, R. Perrino, S. Spagnolo
Vietri sul mare (Italy), May 27th June 1st, 2002
ISBN—88–86409–35–4

Volume XXIX
Workshop on Radiation Dosimetry: Basic Technologies,
Medical Applications, Environmental Applications
Ed.: A. Zanini
Rome (Italy), February 56, 2002
ISBN—88–86409–36–2

Volume XXIX – Suppl.
Workshop on Radiation Dosimetry: Basic Technologies,
Medical Applications, Environmental Applications
Ed.: A. Zanini
Rome (Italy), February 56, 2002
ISBN—88–86409–36–2

Volume XXX – Special Issue
Les Rencontres de Physique de la Vallée d'Aoste –
Results and Perspectives in Particle Physics
Ed.: M. Greco
La Thuile, Aosta Valley, March 9–15, 2003
ISBN—88–86409–39–9

Volume XXXI
Frontier Science 2002 – Charm, Beauty and CP,
First International Workshop on Frontier Science
Eds.: L. Benussi, R. de Sangro, F.L. Fabbri, P. Valente
Frascati, October 6–11, 2002
ISBN—88–86409–37–0

Volume XXXII
19th International Conference on x–ray and Inner–Shell Processes
Eds.: A. Bianconi, A. Marcelli, N.L. Saini
Universitá di Roma La Sapienza June 24–28, 2002
ISBN—88–86409–39–07

Volume XXXIII
Bruno Touschek Memorial Lectures
Ed.: M. Greco, G. Pancheri
Frascati, May 11, 1987
ISBN—88–86409–40–0

Volume XXXIV – Special Issue
Les Rencontres de Physique de la Vallée d'Aoste –
Results and Perspectives in Particle Physics
Ed.: M. Greco
La Thuile, Aosta Valley, February 29 – March 6, 2004
ISBN—88–86409–42–7

Volume XXXV
Heavy Quarks And Leptons 2004
Ed.: A. López
San Juan, Puerto Rico, 1–5 June 2004
ISBN—88–86409–43–5

Volume XXXVI
DAΦNE 2004: Physics At Meson Factories
Eds.: F. Anulli, M. Bertani, G. Capon, C. Curceanu–Petrascu,
F.L. Fabbri, S. Miscetti
Frascati, June 7–11, 2004
ISBN—88–86409–53–2

Volume XXXVII
Frontier Science 2004, Physics and Astrophysics in Space
Eds.: A. Morselli, P. Picozza, M. Ricci
Frascati, 14–19 June, 2004
ISBN—88–86409–52–4

Volume XXXVIII
II Workshop Italiano sulla Fisica di ATLAS e CMS
Eds.: Gianpaolo Carlino and Pierluigi Paolucci
Napoli, October 13 – 15, 2004
ISBN—88–86409–44–3

Volume XXXIX – Special Issue
Les Rencontres de Physique de la Vallée d'Aoste –
Results and Perspectives in Particle Physics
Ed.: M. Greco
La Thuile, Aosta Valley, February 27 – March 5, 2005
ISBN—88–86409–45–1

Volume XL
Frontier Science 2005 – New Frontiers in Subnuclear Physics
Eds.: A. Pullia, M. Paganoni
Milano, September 12 - 17, 2005
ISBN—88–86409–46–X

Volume XLI
Discoveries in Flavour Physics at e^+e^- Colliders
Eds.: L. Benussi, S. Bianco, C. Bloise, R. de Sangro, C. Gatti,
G. Isidori, M. Martini, F. Mescia, S. Miscetti
Frascati, February 28th - March 3rd, 2006
ISBN—88–86409–51–6

Volume XLII – Special Issue
Les Rencontres de Physique de la Vallée d'Aoste –
Results and Perspectives in Particle Physics
Ed.: M. Greco
La Thuile, Aosta Valley, March 5 March 11, 2006
ISBN—88–86409–47–8

Volume XLIII – Special Issue
Neutral Kaon Interferometry at A Phi-Factory: from Quantum Mechanics to Quantum Gravity
Ed.: A. Di Domenico
Frascati, March 24th 2006
ISBN 978—88–86409–50–8

Volume XLIV– Special Issue
Les Rencontres de Physique de la Vallée d'Aoste –
Results and Perspectives in Particle Physics
Ed.: M. Greco
La Thuile, Aosta Valley, February 28, 2 March 5, 2007
ISBN 978—88–86409–49–4

Volume XLV *Frontier Science – Science with the New Generation*
High Energy Gamma-ray Experiments
Eds.: A. Lionetto, A. Morselli
Villa Mondragone, Monteporzio, Italy June 18 -20, 2007
ISBN–978—88–86409–54–0

Volume XLVI
XII International Conference on Hadron Spectroscopy
Eds.: L. Benussi, M. Bertani, S. Bianco, C. Bloise, R. de Sangro, P. de Simone, P. di Nezza, P. Giannotti, S. Giovanella, M.P. Lombardo, S. Pacetti
Laboratori Nazionali di Frascati, October 713, 2007
ISBN—978–88–86409–55–1

Volume XLVII – Special Issue
Les Rencontres de Physique de la Vallée d'Aoste –
Results and Perspectives in Particle Physics
Ed.: M. Greco
La Thuile, Aosta Valley, February 24, 2 March 1st, 2008
ISBN 978–88–86409–56–8